

Chapter 1

Introduction

This chapter gives a brief historical overview of the study of binaries and in doing so explains some of the terminology that is still used. It also gives an outline of the topics that these lecture notes cover.

1.1 History until 1900¹

It has been noted long ago that stars as seen on the sky sometimes occur in pairs. Thus, the star list in the *Almagest* of Ptolemaios, which dates from ± 150 AD, describes the 8th star in the constellation Sagittarius as ‘the nebulous and double ($\delta\pi\lambda\omicron\upsilon\zeta$) star at the eye’. After the invention of the telescope (around 1610) it was very quickly found that some stars that appear single to the naked eye, are resolved into a pair of stars by the telescope. The first known instance is in a letter by Benedetto Castelli to Galileo Galilei on January 7, 1617, where it is noted that Mizar is double.² Galileo observed Mizar himself and determined the distance between the two stars as $15''$. The discovery made its way into print in the ‘*New Almagest*’ by Giovanni Battista Riccioli in 1650, and as a result Riccioli is often credited with this discovery. In a similar way, Huygens made a drawing showing that θ Orionis is a triple star (Figure 1.1), but the presence of multiple stars in the Orion nebula had already been noted by Johann Baptist Cysat SJ³ 1618.

The list of well-known stars known to be double when viewed in the telescope includes the following

year	star	published by	comment
1650	Mizar (ζ UMa)	Riccioli	found earlier by Castelli
1656	θ Ori	Huygens	triple, found earlier by Cysat
1685	α Cru	Fontenay SJ	
1689	α Cen	Richaud SJ	
1718	γ Vir	Bradley	
1719	Castor (α Gem)	Pound	
1753	61 Cygni	Bradley	

¹This Section borrows extensively from Aitken 1935

²see the article on Mizar by the Czech amateur astronomer Leos Ondra on leo.astronomy.cz

³SJ, Societatis Jesu, i.e. from the Society of Jesus: a Jesuit. Jesuits attached great importance to education and science, and in earlier centuries trained good astronomers. Examples are the first European astronomers in China: Ricci (1552-1610) and Verbiest (1623-1688); and the rediscoverers of ancient Babylonian astronomy: Epping (1835-1894) and Kugler (1862-1929)

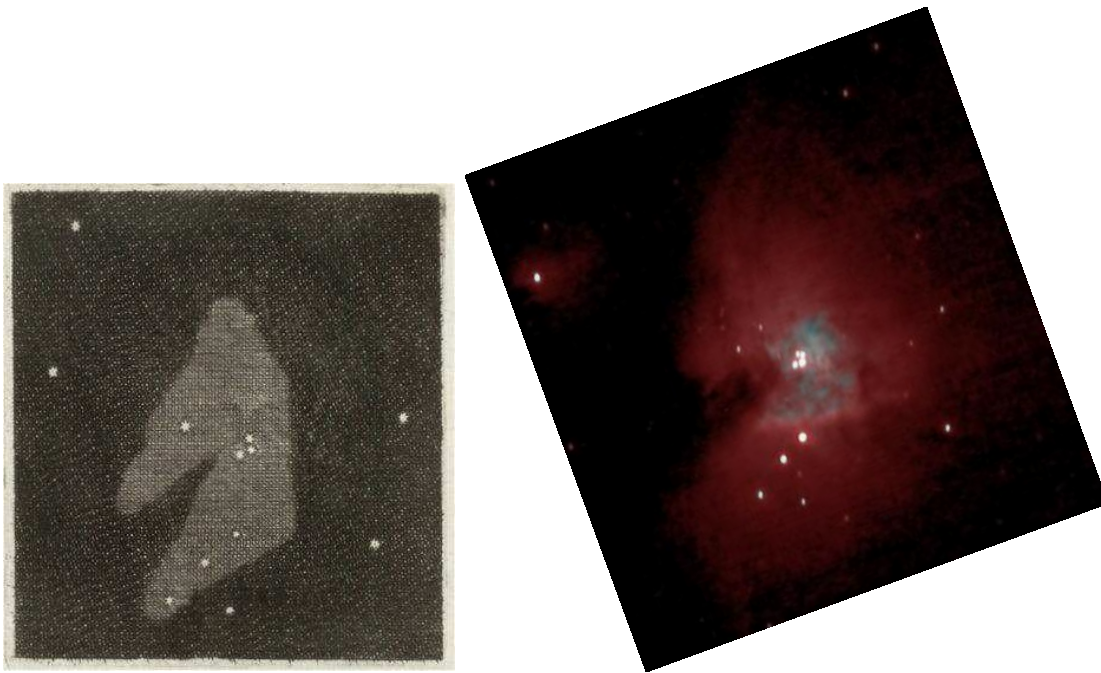


Figure 1.1: *Drawing of the Orion nebula made by Huygens (left) compared with a modern photograph (from www.integram.com/astro/Trapezium.html, right).*

All these doubles were not considered to be anything else than two stars whose apparent positions on the sky happened to be close. Then in 1767 the British astronomer John Michell noted and proved that this closeness is not due to chance, in other words that most pairs are real physical pairs. An important consequence is that stars may have very different intrinsic brightnesses. Michell argues as follows (for brevity, I modernize his notation). Take one star. The probability p that a single other star placed on an arbitrary position in the sky is within x degrees from the first star is given by the ratio of the surface of a circle with radius of x degrees to the surface of the whole sphere: $\pi \times (0.01745x)^2 / (4\pi) \simeq 7.615 \times 10^{-5}x^2$. The probability that it is not in the circle is $1 - p$. If there are n stars with a brightness as high as the faintest in the pair considered, the probability that none of them is within x degrees is $(1 - p)^n \simeq 1 - np$. Since for the first star we also have n choices, the probability of no close pair anywhere in the sky is $(1 - p)^{n \times n} \simeq 1 - n^2p$. As an example, Michell considers β Capricorni, two stars at $3'20''$ from one another, i.e. $x = 0.0555$, with $n = 230$. The probability of one such a pair in the sky due to chance is 1 against 80.4. With a similar reasoning, Michell showed that the Pleiades form a real star cluster.

*visual
binary
statistical*

As an aside, we consider the Bright Star Catalogue. For each star in this catalogue, we compute the distance to the nearest (in angular distance) other star, and then show the cumulative distribution of nearest distances in Figure 1.2. (Stars in the catalogue with the exact position of another star, or without a position, have been removed from this sample.) We then use a random generator to distribute the same number of stars randomly over the sky, and for these plot the cumulative nearest-distance distribution in the same Figure. It is seen that the real sky has an excess of pairs with distances less than about 0.1° .

Starting in 1779 William Herschel compiled a list of close binaries. In doing so he was following an idea of Galileo: if all stars are equally bright, then a very faint

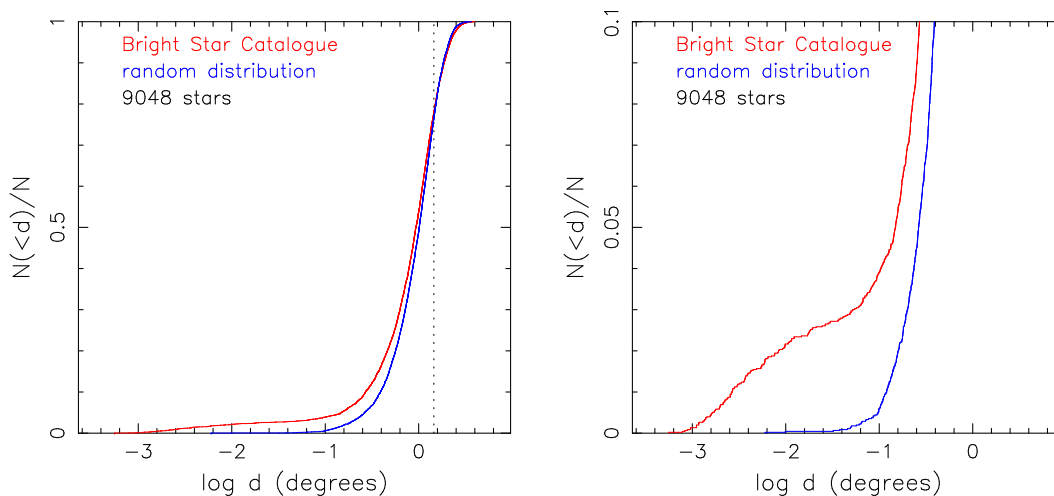


Figure 1.2: *Cumulative distribution of the angular distance to the nearest star for the stars in the Bright Star Catalogue (only stars with an independent catalogued position are included), and for the same number of stars distributed randomly over the sky.*

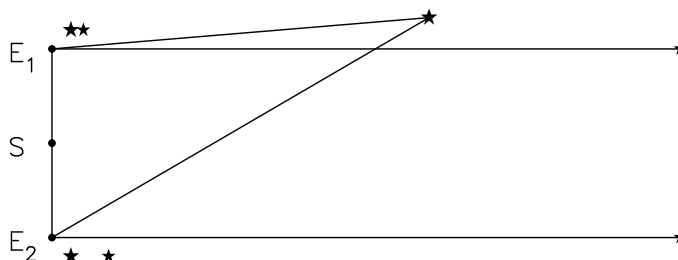


Figure 1.3: *Illustration of Galileo’s idea of measuring the parallax from a close pair of stars. If all stars are equally bright intrinsically, the fainter star is much further than the brighter star, and its change in direction as the Earth (E) moves around the Sun (S) negligible with respect to that of the brighter star. The figure shows the change in relative position as the Earth moves from E_1 to E_2 half a year later.*

star next to a bright one must be much further away. From the annual variation in angular distance between the two stars, one can then accurately determine the parallax of the nearer, brighter star (Figure 1.3). Herschel found many such pairs, which he published in catalogues. He notes that close pairs can be used to test the quality of a telescope and of the weather (Herschel 1803).

Herschel first assumed that the double stars are not physical, but soon realised that most must be physical pairs, and then defined single and double stars (Herschel 1802):

When stars are situated at such immense distances from each other as our sun, Arcturus, Capella, Sirius, Canobus (sic), Markab, Bellatrix, Menkar, Shedir, Algorah, Propus, and numerous others probably are, we may then look upon them as sufficiently out of reach of mutual attractions, to deserve the name of insulated stars.

If a certain star should be situated at any, perhaps immense, distance behind another, and but very little deviating from the line in which we see

the first, we should then have the appearance of a double star. But these stars, being totally unconnected, would not form a binary system. If, on the contrary, two stars should really be situated very near each other, and at the same time so far insulated as not to be materially affected by the attraction of neighbouring stars, they will then compose a separate system, and remain united by the bond of their own mutual gravitation towards each other. This should be called a real double star; and any two stars that are thus mutually connected, form the binary system which we are now to consider.

It is easy to prove, from the doctrine of gravitation, that two stars may be so connected together as to perform circles, or similar ellipses, round their common centre of gravity. In this case, they will always move in directions opposite and parallel to each other; and their system, if not destroyed by some foreign cause, will remain permanent.

Chapter 2.1

Apparently unaware of Michell's earlier work, Herschel computed the probability of getting a pair of stars with magnitudes 5 and 7, respectively, within 5'' of one another, given the numbers of stars with magnitudes 5 and 7. He concluded that such close pairs are real binaries.

Herschel observed α Geminorum, also known as Castor, between November 1779 and March 1803. The less luminous of the two stars was to the North, and preceding (i.e. with smaller right ascension) during this time, and to the accuracy of Herschel's measurements always at the same distance of the brighter star. By taking multiple observations on the same day, he obtained an estimate of the error with which he determined the positional angle: under ideal circumstances somewhat less than a degree. He used an observation by Bradley in 1759, confirmed by Maskelyne in 1760, that the two stars of Castor were in line with the direction between Castor and Pollux, to extend his time range. Herschel gives his data only in tabular form; plots of his values are given in Figure 1.4. For a circular orbit, Herschel concludes from the change between 1759 and 1803 that the binary period is about 342 years and two months (a modern estimate is 467 yrs; see Table 3.1). Herschel argues that it is virtually impossible that three independent rectilinear motions of the sun and the two stars of Castor produce the observed apparent circular orbit. He strengthens the argument by considering five other binaries, viz. γ Leonis, ϵ Bootis ('This beautiful double star, on account of the different colours of the stars of which it is composed'), ζ Herculis, δ Serpentis and γ Virginis.

*visual
binary
individual*

The list of close pairs of stars increased with time, and some astronomers specialised in finding them. In Dorpat (Estonia) Frederick Struve systematically scanned the sky between the North pole and -15° , examining 120 000 stars in 129 nights between November 1824 and February 1827. With bigger telescopes, close pairs were increasingly found. Therefore the lists of binaries became longer and longer, especially after John Herschel's suggestion was followed to include individual measurements of angular distance and position angle with the date of observation. Flammarion's selection of only those pairs where orbital motion had been observed was very helpful.

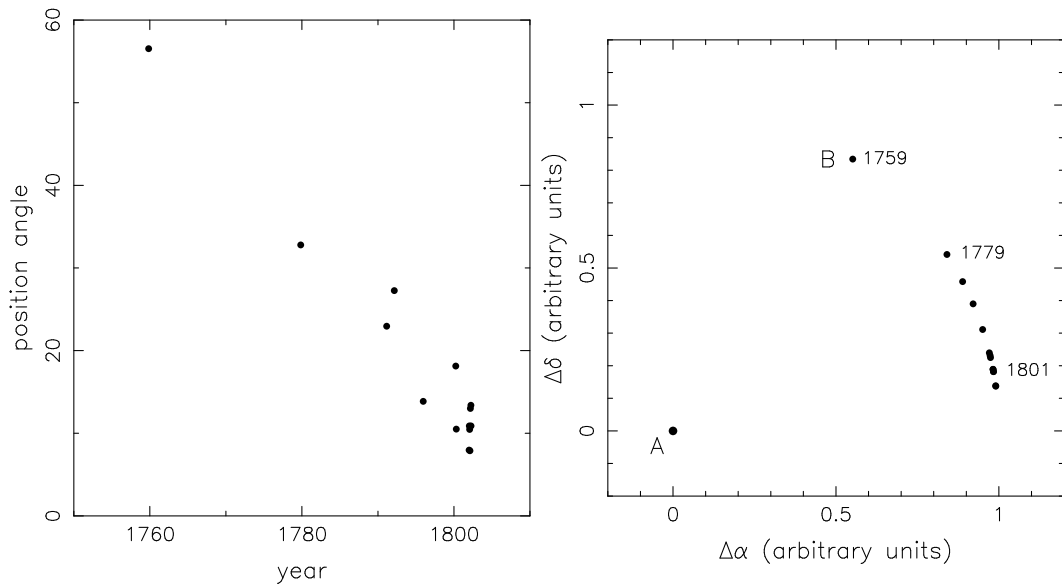


Figure 1.4: *William Herschel observed the position angle of the two stars in Castor between 1779 and 1803; and added a measurement by Bradley from 1759, and discovered the motion of the two stars in the binary orbit.*

year	astronomer	N_{bin}	comment
1779	Mayer	80	faint companions to bright stars
1784	W. Herschel	703	
1823	J. Herschel & J. South	380	southern sky
1827	Struve	3110	
1874	J. Herschel	10 300	published posthumously
1878	Flammarion	819	only pairs with observed binary motion

The micrometer, invented by W. Herschel, was continuously improved so that measurements of angular distances and position angles became increasingly accurate. Further improvements came with photography, which, as Hertzsprung remarked, provides a ‘permanent document’. The first binary to be photographed, in 1857 by Bond, was... Mizar.

Methods to derive the orbital parameters from a minimum of 4 observations were developed by Savary (1830), Encke (1832), and J. Herschel (1833), and many others. In these methods, an important consideration is to minimize the number of computations; as a result they are now only of historic interest.

Meanwhile another binary phenomenon had gradually been understood. In 1670 Geminiano Montanari had discovered that the star β Persei varies in brightness. β Persei is also called Algol, ‘the Demon’, the Arabic translation of Ptolemy’s Medusa, whose severed head Perseus is holding⁴. John Goodricke discovered in 1782 that the variation is periodic, with about two-and-a-half days (modern value: 2.867 d), and suggested as one possibility that the darkening was due to the passage

*eclipsing
binary*

This suggestion was spectacularly confirmed when a third method of studying

⁴Contrary to what has been asserted, therefore, the name Algol does not suggest that the Arabic astronomers already knew about the variability.

binaries was implemented: the measurement of radial velocity variations. In 1889 Pickering showed that the spectral lines of . . . Mizar doubled periodically, reflecting Doppler variations due to the orbital motion. In the same year Vogel showed that the spectral lines of Algol were shifted to the red before the eclipse, and to the blue after the eclipse, and thereby confirmed the eclipse interpretation of Goodricke. A binary in which the orbital variation is observed in the spectral lines of both stars, like Mizar, is called a *double-lined spectroscopic binary*, if the spectral lines of only one star are visible in the spectrum, we speak of a *single-lined spectroscopic binary*. *spectroscopic binary*
single- or doublelined

It is now known that the spectroscopic period of Mizar is 20.5 d, much too short for the two stars that Castelli and Galileo observed through their telescopes and that Bond photographed. In a visual binary, the brighter star is usually (but confusingly not always) referred to as star A, the fainter one as star B. The 20.5 d period shows that Mizar A is itself a binary. Mizar B is also a binary, with a 175.6 d period.

The first catalogue of spectroscopic binaries was published in 1905 by Campbell, with 124 entries. The catalogue that Moore published in 1924 already had 1054 entries. Methods for deriving the binary parameters were devised by Rambaut in 1891, and by Lehman-Filhés in 1894. Soon the number of orbits determined from spectroscopy surpassed the number of visually determined orbits. The reason is straightforward: spectroscopic orbits must be short to be measurable, a visual orbit long. Therefore a spectroscopic orbit can be found in a shorter time span. Equally important is that a spectroscopic binary can be detected no matter what its distance is, whereas the detection of visual orbits requires nearby binaries.

1.2 Lightcurves and nomenclature

As the number of eclipsing binaries grew, different types were discriminated. The simplest type, often called the Algol type, shows two eclipses per orbit, of which the deeper one is called the primary eclipse. To interpret this, consider a binary of a hot and a cold star. When the cold star moves in front of the hot star, the eclipse is deep, and when the hot star moves in front of the cool star, the eclipse is shallow. *primary eclipse*

When the two stars in a binary are far apart and non-rotating, they are spherical, and thus the lightcurve is flat between the eclipses. When the stars are closer they are deformed under the influence of one another, elongated along the line connecting the centers of the two stars. Thus the surface area that we observe on earth is largest when the line of sight to the Earth is perpendicular to the line connecting the two stars, and this is reflected in a lightcurve that changes throughout the orbit. Such variations are called *ellipsoidal variations*. When both stars touch, their deformation causes large variations throughout the orbit. To describe the form of the stars under the influence of one another's gravity, we must compute the equilibrium surfaces in the potential of two stars: the *Roche geometry*. *ellipsoidal variations*
Chapter 3.4

The study of lightcurves showed up more and more details, or complications, depending on your point of view. . . .

Thus, if one small star disappears for a time behind a bigger star, the minimum of its eclipse is flat (i.e. of constant flux). Clearly, the length of ingress and egress, and of the bottom of the eclipse, contain information on the relative sizes of the two binary stars. Rapidly rotating stars are flattened, leading to different eclipse forms. Stars can have variable spots on them, leading to variable lightcurves. Gas can flow from one star to the other, leading to asymmetric lightcurves, and in fact also to **Chapter 4.3.1**
rotation spots gas streams

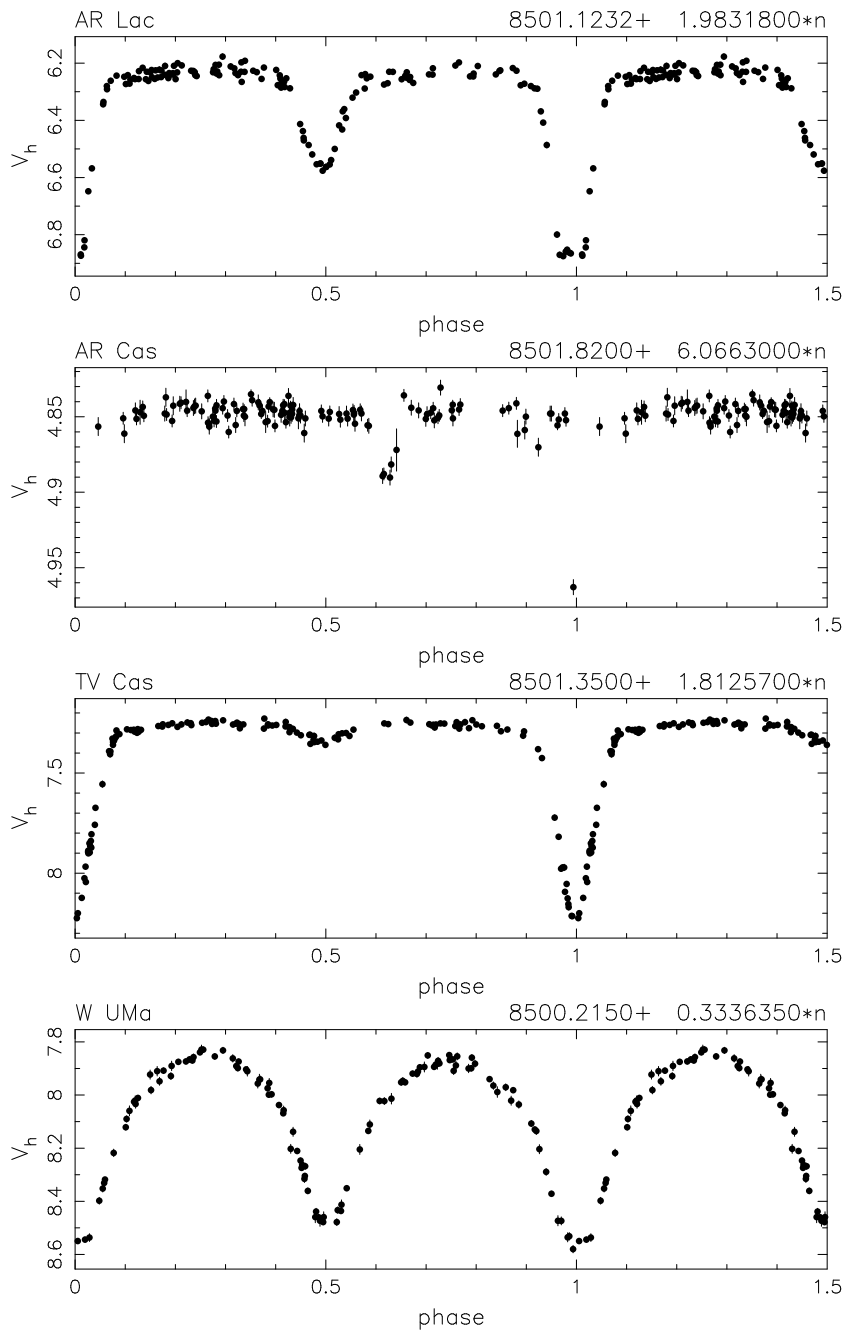


Figure 1.5: *Various examples of lightcurves, taken from the Hipparcos Catalogue. One-and-a-half orbital period is shown for each star. The top curve shows two eclipses per orbit, separated by half the orbital period; the curve of AR Cas shows two eclipses asymmetrically located over the orbital period. TV Cas shows ellipsoidal variations, and the contact binary W UMa even more so.*

asymmetric radial velocity curves, even in circular orbits. A hot star may heat the facing surface of its companion, thus reducing or even inverting the light changes when the companion is eclipsed. In the course of the 20th century observations and interpretation of radial velocity curves and lightcurves were continuously improved. The variation in interpretation also led to a proliferation of names for various binary types, usually after a prototype.

So one can encounter statements like ‘AR Lac is an RS CVn variable’, or ‘AR

Cas is an Algol type variable'. To understand this we make a short digression into nomenclature. To designate variable stars, Argelander introduced the following, alas rather convoluted, system. The first variable discovered in a constellation Con is called R Con, the second one S, the third one T and so on to Z. Argelander thought that variability was so rare, that this would be enough. It isn't! and one continues with RR, RS, ... RZ, SS, ST, ... SZ to ZZ. After that follows AA, AB, ... AZ, BB, BC, ... BZ, etc. until QZ. The letter J is not used (probably for fear of confusion with I). After this, one starts enumerating: V335 Con, V336 Con, etc., where V stands for variable. So we now know that AR Lac is the 71th variable discovered in the constellation Lacerta.

*nomenclature
variable
stars*

Thus, eclipsing binaries often have a designation as a variable star. It should be noted, however, that many variable stars are not binaries; most are pulsating variables, like RR Lyrae, some are magnetically active stars, like the flare star UV Ceti, and some are young stars with the forming disk still present, like T Tau.

The number of prototypes after which a class of objects is named is rather large; in general the World Wide Web is the best place to start finding out what type of star the prototype is. We will encounter designations of particular classes of binaries throughout these lecture notes, but two may be mentioned here. A short-period binary in which one star has evolved into a subgiant or giant, whereas the other is still on the main sequence, is called an RS CVn type variable. Such binaries are often eclipsing, and further stand out through magnetic activity that causes stellar spots and X-ray emission. When the giant expands, it may at some point start transferring mass to its companion: it has then become an Algol system.

*RS CVn
type*

Algol type

The maximum size that a star can have before gas flows over from its surface to the other star is called the *Roche lobe* (Roche 1859⁵). When a star fills its Roche lobe, one expects in most cases that tidal forces have circularized the orbit.

Chapter 9
*Roche-lobe
overflow*

The relatively recent physical classification of a binary does not always agree with the old lightcurve nomenclature. The statement 'AR Cas is an Algol type variable' is a good example. From Figure 1.5 we see that the orbit of AR Cas is eccentric: thus, the giant presumably does not fill its Roche lobe in this system, as also indicated by the absence of ellipsoidal variations, and AR Cas is better classified as an RS CVn system.

An often used classification of binaries refers to the sizes of the stars with respect to their Roche lobes. If both stars are smaller than their Roche lobe, the binary is *detached*. If one star fills its Roche lobe, the binary is *semi-detached*; if both stars fill or over-fill their Roche lobes, i.e. the stars touch, the binary is a *contact binary*, also called a W UMa system, after its prototype.

*detached,
semi-
detached,
contact*

It is very difficult to determine from the lightcurve alone whether a star is just close to filling its Roche lobe, or actually fills it. For this reason, a classification of lightcurves based on this distinction, i.e. EA for detached, EB for semidetached, and EW for contact, is becoming obsolete. Nonetheless, clearly separated stars are easily recognisable from the absence of ellipsoidal variations and from the eccentricity of the orbit (as derived from the unequal time intervals between the primary and secondary eclipse), e.g. AR Cas in Figure 1.5; and contact binaries from the strong variation of the lightcurve throughout the orbit, e.g. W UMa in Figure 1.5.

EA, EB, EW

⁵Roche computed the maximum size of the atmosphere of a comet before the Sun disrupts it!

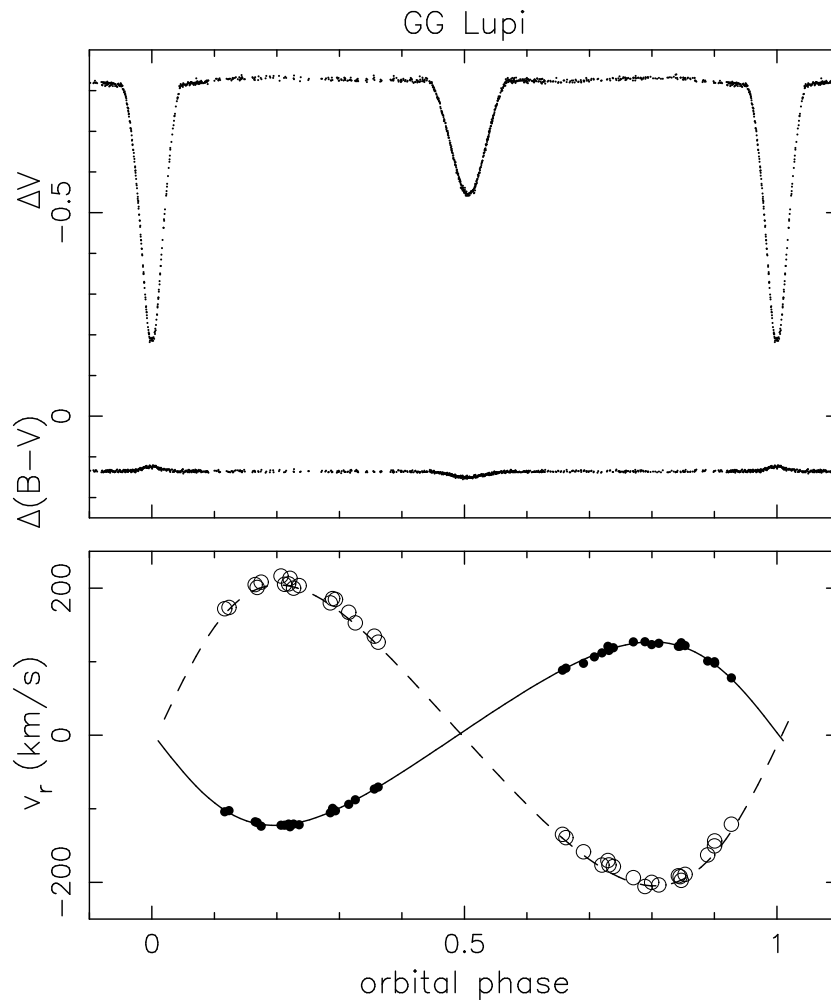


Figure 1.6: *Lightcurves and radial-velocity curves of the binary GG Lup (B7 V + B9 V). The orbital period is 1.85 d. In the lightcurves the changes of V and B–V with respect to a constant comparison star are plotted. In the radial-velocity plot the theoretical curves have been added to the observed data points for the more massive star (•, solid line), and for the lighter star (◦, dashed line). After Clausen et al. (1993) and Andersen et al. (1993).*

1.3 The development of modern binary research

In the 20th century more and more data were gathered from binaries, in studies of the orbits of *visual binaries*, the velocities of *spectroscopic binaries*, and the flux variations of *eclipsing binaries*. An important development in the 1970s followed the design of the velocity correlator by Griffin. The standard way to measure a stellar velocity is to obtain a high-quality, high-resolution spectrum, and then fit the spectral lines. This requires large amounts of observing time on large telescopes. The velocity correlator works as follows (Griffin 1967):

*velocity
correlator*

Suppose a widened spectrogram is obtained, through the optics of a spectrometer, of, say, a bright K star; and that it is returned after processing to the focal surface where it was exposed, the telescope being turned to the same star. If the spectrogram is replaced accurately in register with the stellar spectrum, all the bright parts of the spectrum will be systemat-

ically obstructed by heavily exposed emulsion, and rather little light will pass through the spectrogram. If it is not in register, the obstruction of the spectrum will not be systematic and the total transmission will be greater.

The spectrum can be used for the measurement of velocities of other stars, simply by measuring the transmitted light as a function of the position, regulated with a screw. With this instrument, radial velocities with an accuracy as good as 1 km/s can be obtained in relatively short observing times. Slightly modified versions of the velocity correlator were made for a number of telescopes, and became the work horses for long-term studies of spectroscopic binaries. For the first time, systematic studies of the binary frequency in stars near the Sun, and of stars in selected stellar clusters, became possible. In particular Mayor and his collaborators of the Observatoire de Genève contributed to these studies with the CORAVEL.

The work horse of choice for many years for the fitting of lightcurves and radial velocities was the computer code developed by Wilson & Devinney. It computed which surface elements of the two stars in a binary were visible at each orbital phase, and added the fluxes from these elements. Often, the spectrum of each element was taken to be a black body spectrum, and colour corrections to stellar spectra were made only for the summed flux and colours. For spherical stars the analysis is relatively straightforward, but for a deformed star one must take into account that the measured radial velocity may not reflect the velocity of the centre of mass. An example of data of high quality, allowing the determination of masses, radii and luminosities to within a few percent, is given in Figure 1.6.

The theory of binaries came into being with the understanding of the evolution of stars, the first ideas of which were developed in the 1920s by Eddington. Main sequence stars evolve into giants, and giants leave white dwarfs upon shedding their envelope. Massive giants can shed their envelope in a supernovae explosion and leave a neutron star or a black hole. The study of binaries is an important aspect of the study of stellar evolution, as it provides accurate masses and radii, for comparison with stellar evolution. It also may pose questions that stellar evolution has to answer. A nice example is the Algol paradox.

From stellar evolution, we know that the more massive star in a binary evolves first. It was therefore a nasty surprise when it was discovered that the giant in Algol systems is usually less massive than its unevolved companion! This ‘Algol paradox’ was solved by Kuiper (1941), when he realized that mass is being transferred from the giant to its main-sequence companion: apparently enough mass has already been transferred that the initially more massive star has become the less massive star by now. The evolution of such binaries under the influence of mass transfer has been described in the 1960s in a number of classical papers by Paczyński and by Kippenhahn & Weigert. Our understanding of stellar evolution, and by extension, of the evolution of binaries continues to increase as our understanding of for example opacities, the equation of state, and nuclear reactions continues to be improved.

From the observational point of view the end of the 20th century saw a number of very large changes, which have completely transformed astronomy in general, and the studies of binaries in particular.

Space research made it possible to study stars at previously inaccessible wavelengths: ultraviolet and X-rays, and more recently infrared. The shorter wavelengths

Chapter 3.4.1
*Wilson &
Devinney
code*

Chapter 3.3

Chapter 4

*Algol para-
dox*

Chapter 9,10

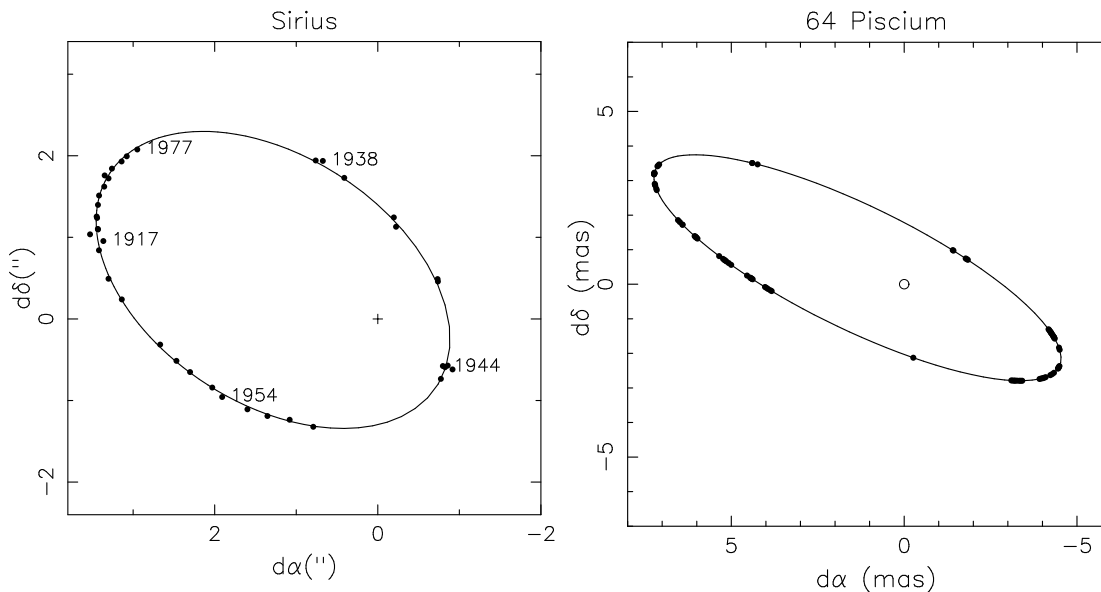


Figure 1.7: *Left: orbital motion of Sirius A with respect to a fixed point on the sky (+, after correction for proper motion). The orbital period is 50.09 yr. Right: the 13.8 d orbit of 64 Piscium with respect to its companion (●) is resolved with the Palomar Testbed Optical Interferometer. After Gatewood & Gatewood (1978) and Boden et al. (1999).*

started the wholly new topic of the study of binaries with neutron stars and black holes, and greatly extended the research of binaries with white dwarfs.

Chapter 12

Larger telescopes became possible with the technology of supporting thin mirrors with a honeycomb structure, thus allowing mirrors of 8 m diameter.

Optical interferometers became possible when technology allowed distances between mirrors to be regulated with an accuracy better than one-tenth of the wavelength of observation: i.e. first in the infrared. The technique has been pioneered by Michelson in the beginning of the 20th century, and allowed Pease (1927) to make the first interferometric resolution of a binary, viz. . . . Mizar A. In the last decades of the 20th century, routine interferometric measurements became possible, allowing milliarcsecond resolution (e.g. Figure 1.7).

Infrared detectors opened up the field of pre-main-sequence stars (Figure 1.8).

CCD cameras allow much more rapid observations, which can be calibrated much more easily than photographic plates. This allows standard photometry with an accuracy of 1% or better, and rapid spectroscopy. It also makes the data immediately available in digital format

Computers allow the handling of much larger data sets, and the correct handling of them. In earlier studies, fitting of radial velocity data and of visual orbits had to be done in an approximate fashion, often not allowing realistic error estimates. With computers, a much more correct way of data analysis and fitting is possible. The development of *software* is an important aspect of this: a good example is the Munich Interactive Data Analysis System MIDAS.

Computers also allow much more detailed computation of the evolution of single stars, and by extension of binaries. They also allow more accurate computation of stellar atmosphere models, for comparison with light curves.

The combination of these developments leads to other advances:

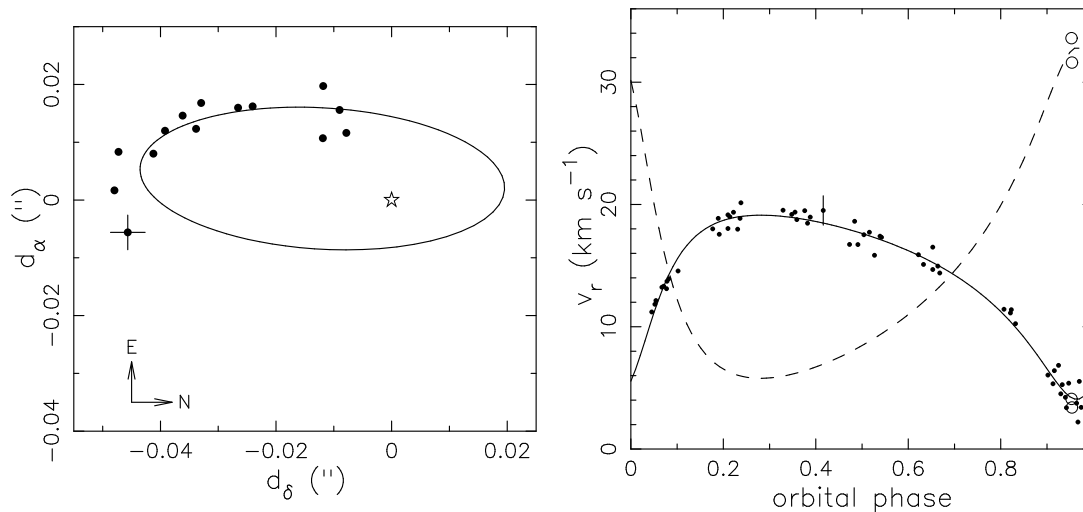


Figure 1.8: *Visual orbit and radial velocity curve of the T Tau star 045251+3016 in the Taurus Auriga star forming region. After Steffen et al. (2001)*

Data bases can be constructed much more easily now that the data are often digital from the start. They require much storage space, and thus large computers. The World Wide Web allows access to many of these data bases, including standardized analysis software.

Velocity Correlation for CCD spectra can be done on the computer: the spectrum of the object can be compared to a whole library of (observed or theoretical) stellar spectra, allowing not only the determination of the velocity, but also of stellar spectrum parameters as temperature, gravity, and metallicity. Radial velocities can now be measured with an accuracy less than 10 m/s, depending on the stellar type.

Lightcurve fitting. With the faster computers today it is possible to fit a stellar spectrum directly to each surface element; this is important because it allows correct application of limb-darkening. With the more accurate CCD data, more orbital phases can be studied. With genetic algorithms, all parameters can be fitted simultaneously.

Visibility fitting. An interferometer measures the interference pattern between different sources of light, e.g. the two stars in a binary, combined from several apertures, i.e. the separate mirrors of the interferometer. The strength of the interference is expressed as the *visibility* and depends on the angular distance between the two stars, and on the distances between the mirrors of the interferometer. Rather than first derive the angular distance and position angle of the stars, and then fit these, one can now directly fit the observed visibilities.

Automated or semi-automated observations have led to an important role of small telescopes. Typically, a small telescope surveys the sky, and discovered an object with interesting variability or colour. A followup with a 1 m telescope then may give a better lightcurve, and if the system is still deemed interesting a radial velocity curve is obtained with an 8 m telescope. This type of observations has led to the determination of accurate masses and radii of very-low-mass stars and of brown dwarfs.

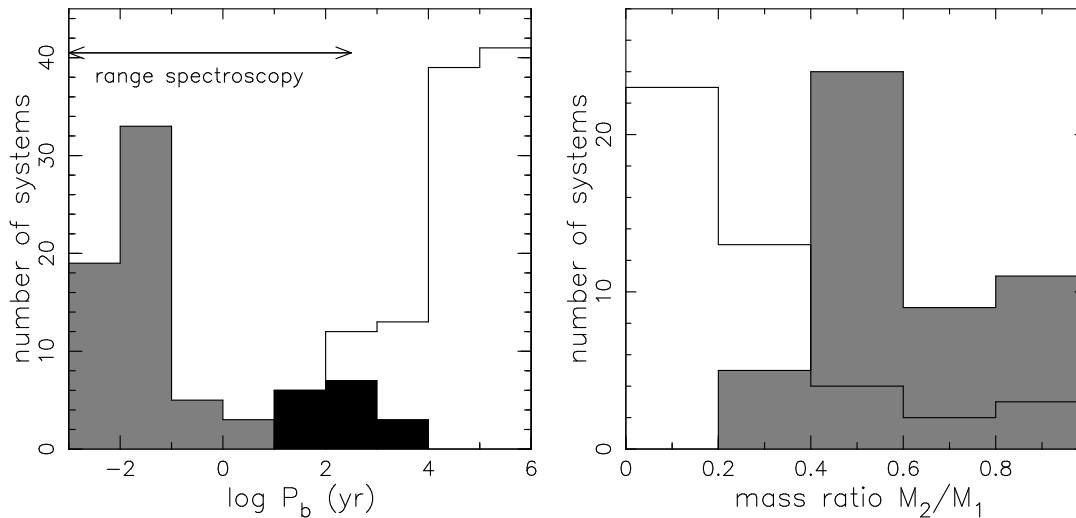


Figure 1.9: *Distribution of orbital periods (left) and mass ratios (right) of O stars as observed (i.e. not corrected for selection effects). Spectroscopic binaries are indicated with gray, visual binaries with white, and speckle binaries with black histograms. After Mason et al. (1998)*

1.4 These lecture notes

This Lecture Course is set up as follows. First we derive the relative orbit of two stars under the influence of their mutual gravitation (Chapter 2), and then we derive the visual orbit, the radial velocity curve, and the eclipse lightcurve for a binary observed from Earth (Chapter 3). We briefly indicate how observations can be fitted to these theoretical curves. In these chapters we assume perfectly spherical masses. In Chapter 4 we show how parameters of binaries are derived from the observations, and discuss a number of interesting cases. In Chapter 5 we discuss perturbations: how a star becomes non-spherical under the influence of its companion, how this affects the observed orbital variations of flux and velocity, and how the deformation affects the orbit.

In Chapter 6 we discuss a special binary: the Earth-Moon binary planet. Even though some of the properties of a binary of (mostly) solid objects differ from those of a binary of gaseous stars, some of the results derived in this Chapter apply to binaries in general. For Chapters 7 and 8, on the evolution of a binary under the influence of tidal forces, we use two articles by Piet Hut.

In Chapter 9 we start discussing interacting binaries, in which mass is (or has been) transferred from one star to the other. We discuss the stability of mass transfer and derive the effects of mass transfer on the evolution of the orbit. In Chapter 10 we discuss binaries in which mass is transferred in different evolutionary stages of the mass donor: the main sequence and the first giant branch. In Chapter 11 we discuss rapid changes of a binary, due to a supernova explosion or due to one star entering the envelope of its companion star. In Sections 12 and 13 we discuss binaries with compact objects.

1.5 Exercises

The following sites may be useful:

general information on astronomical objects simbad.u-strasbg.fr this site also has links to catalogues.

popular site on stars www.astro.uiuc.edu/~kaler/sow/

reference search adsabs.harvard.edu/abstract_service.html

Exercise 1. Use the Web to find the Bayer names for the stars Markab, Algorah and Propus mentioned in the quotation on page 3 from Herschel.

Exercise 2. Use SIMBAD and the Hipparcos Catalogue to find the distance to Mizar. Noting that Galileo measured the distance between Mizar A and B as 15", give a rough estimate of the orbital period.

Exercise 3. Get the pdf-file of the paper in which Herschel gives his measurements of the orbit of Castor AB; and of the paper in which Griffin explains the velocity correlation method.

Exercise 4. Confirm from the lightcurves of GG Lup (Figure 1.6) that the primary eclipse is the eclipse of the hotter star.

Exercise 5. Consider a binary of two O stars, each with a mass of $20 M_{\odot}$. The nearest O stars are at about 250 pc. With an angular resolution of 0.1" and a radial velocity accuracy of 5 km/s, determine the minimum period for studying this binary as a visual binary, and the maximum period for studying its radial-velocity curve. Assume that a reliable study requires an amplitude 5 times bigger than the measurement accuracy. Compare the results with Figure 1.9. How do the limits change when the accuracy is improved by a factor 100 (as has happened since 1980)?

1.6 References with the Historical Introduction

this list is as yet incomplete.

1. R.G. Aitken. *The binary stars*. Reprint in 1964 by Dover Publications, New York, 1935.
2. A. Boden, B. Lane, M. Creech-Eakman et al. The visual orbit of 64 Piscium *ApJ*, 527:360–368, 1999.
3. J. Andersen, J. Clausen, A. Gimenez. Absolute dimensions of eclipsing binaries, XX. GG Lupi: young metal-deficient B stars. *AA*, 277:439–451, 1993.
4. J. Clausen, J. Garcia, A. Gimenez, B. Helt, L. Vaz. Four colour photometry of eclipsing binaries, XXXV. Lightcurves of GG Lupi: young metal-deficient B stars. *AAS*, 101:563–572, 1993.
5. G. Gatewood and C. Gatewood A study of Sirius *ApJ*, 225:191–197, 1978.
6. J. Goodricke. On the periods of the changes of light in the star Algol. *Philosophical Transactions*, 74:287–292, 1784.
7. R.F. Griffin. A photoelectric radial-velocity spectrometer. *ApJ*, 148:465–476, 1967.
8. W. Herschel. Catalogue of 500 new nebulae, nebulous stars, planetary nebulae, and clusters of stars; with remarks on the construction of the heavens. *Philosophical Transactions*, 92:477–528, 1802.

9. W. Herschel. Account of the changes that have happened, during the last twenty-five years, in the relative situation of double-stars; with an investigation of the causes to which they are owing. *Philosophical Transactions*, 93:339–382, 1803.
10. R. Kippenhahn. Mass exchange in a massive close binary system. *A&A*, 3:83–87, 1969.
11. R. Kippenhahn and A. Weigert. Entwicklung in engen Doppelsternsystemen. I. Massen- austausch vor und nach Beendigung des zentralen Wasserstoff-Brennens. *Zeitschr. f. Astroph.*, 65:251–273, 1967.
12. G.P. Kuiper. On the interpretation of β Lyrae and other close binaries. *ApJ*, 93:133–177, 1941.
13. B. Mason, D. Gies, W. Hartkopf, W. Bagnuolo, Th. ten Brummelaar, and H. McAlister. ICCD speckle observations of binary stars. XIX. An astrometric spectroscopic survey of O stars. *AJ*, 115:821–847, 1998.
14. J. Michell. An inquiry into the probable parallax, and magnitude of the fixed stars, from the quantity of light which they afford us, and the particular circumstances of their situation. *Philosophical Transactions*, 57:234–264, 1767.
15. B. Paczyński. Evolution of close binaries. I. *Acta Astron.*, 16:231, 1966.
16. B. Paczyński. Evolution of close binaries. IV. *Acta Astron.*, 17:193–206 & 355–380, 1967.
17. F.G. Pease. Interferometer Notes. IV. The orbit of Mizar. *PASP*, 39:313–314, 1927.
18. G.B. Riccioli. *Almagestum novum, astronomiam veterem novamque complectens: observationibus aliorum, et propriis novisque theorematibus, problematibus, ac tabulis promotam*. Victorius Benatius, Bononia (=Bologna), Vol.1 Part 1, p.422, 1651.
19. É. Roche. Recherches sur les atmosphères des comètes. *Annales de l'Observatoire imperial de Paris*, 5:353–393, 1859.
20. A. Steffen, R. Mathieu, M. Lattanzi, et al. A dynamical mass constraint for pre-main-sequence evolutionary tracks: the binary NTT 045251+3016 *AJ*, 122:997–1006, 2001.

Chapter 2

The gravitational two-body problem

In this chapter we derive the equations that describe the motion of two point masses under the effect of their mutual gravity, in the classical Newtonian description.

2.1 Separating motion of center of mass and relative orbit

Suppose we have two masses, M_1 at position \vec{r}_1 and M_2 at position \vec{r}_2 . The equations of motion for the two bodies are

$$M_1 \ddot{\vec{r}}_1 = - \frac{GM_1 M_2}{|\vec{r}_1 - \vec{r}_2|^2} \vec{e}_{12} \quad (2.1)$$

$$M_2 \ddot{\vec{r}}_2 = + \frac{GM_1 M_2}{|\vec{r}_1 - \vec{r}_2|^2} \vec{e}_{12} \quad (2.2)$$

where a dot \cdot denotes a time derivative, and where \vec{e}_{12} is a vector of unit length in the direction from M_2 to M_1 .

We now define two new coordinates, one denoting the center of mass:

$$\vec{R} \equiv \frac{M_1 \vec{r}_1 + M_2 \vec{r}_2}{M_1 + M_2} \quad (2.3)$$

and one the vector connecting the two masses:

$$\vec{r} \equiv \vec{r}_1 - \vec{r}_2 \quad (2.4)$$

Adding equations 2.1 and 2.2 gives

$$M_1 \ddot{\vec{r}}_1 + M_2 \ddot{\vec{r}}_2 = 0 \quad \Rightarrow \quad \ddot{\vec{R}} = 0 \quad (2.5)$$

which implies that the center of mass has a constant velocity:

$$\dot{\vec{R}} = \text{constant vector} \quad (2.6)$$

Dividing Eqs. 2.1 and 2.2 by M_1 and M_2 , respectively, and subtracting the results, one obtains

$$\ddot{\vec{r}}_1 - \ddot{\vec{r}}_2 = - \left(\frac{1}{M_1} + \frac{1}{M_2} \right) \frac{GM_1 M_2}{|\vec{r}_1 - \vec{r}_2|^2} \vec{e}_{12} \quad \Rightarrow \quad \mu \ddot{\vec{r}} = - \frac{GM_1 M_2}{r^3} \vec{r} \quad (2.7)$$

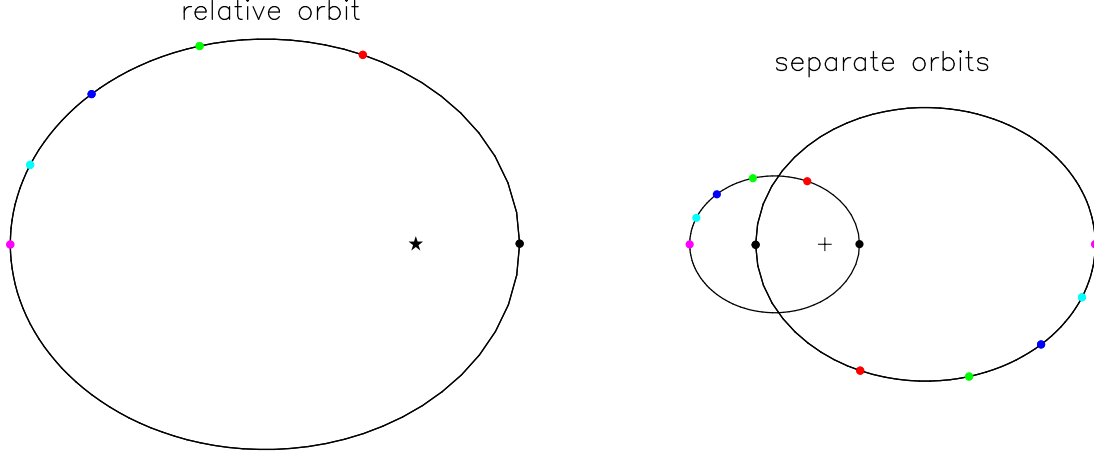


Figure 2.1: Relation between the relative orbit (left) and absolute orbits (right) of a binary, in this case Sirius, as expressed by Eq. 2.9.

where we have introduced the *reduced mass*:

$$\mu = \frac{M_1 M_2}{M_1 + M_2} \quad (2.8)$$

We have now split the equations of motion 2.1 and 2.2 into an equation 2.6 for the motion of the center of mass, and an equation 2.8 for the motion of the vector connecting the masses. To see how the vectors for the masses \vec{r}_1 and \vec{r}_2 can be obtained once we have solved Eq. 2.7, we solve Eqs. 2.3 and 2.4 for them:

$$\vec{r}_1 = \vec{R} + \frac{M_2}{M_1 + M_2} \vec{r} \quad ; \quad \vec{r}_2 = \vec{R} - \frac{M_1}{M_1 + M_2} \vec{r} \quad (2.9)$$

From this equation we learn that the orbits of M_1 and M_2 with respect to the center of mass have the same form, and that the sizes of the orbits are inversely proportional to the masses.

Consider the angular momentum of a particle with mass μ :

$$\vec{L} \equiv \mu \vec{r} \times \dot{\vec{r}} = \text{constant vector} \quad (2.10)$$

where \times denotes the outer product. That the angular momentum is constant, follows from its time derivative, noting that the force is along the line connecting the masses, $\vec{r} \parallel \ddot{\vec{r}}$ (Eq. 2.7):

$$\dot{\vec{L}} = \mu \left(\dot{\vec{r}} \times \dot{\vec{r}} + \vec{r} \times \ddot{\vec{r}} \right) = 0 \quad (2.11)$$

Thus the angular momentum vector \vec{L} is conserved, and has a fixed direction, perpendicular to both \vec{r} and $\dot{\vec{r}}$. This implies that the orbital plane of both masses is fixed, perpendicular to the angular momentum vector. We can therefore describe the motion of the masses with two coordinates, in this plane. For these coordinates we choose cylindrical coordinates r and ϕ , which lead to

$$\dot{\vec{r}} = \dot{r} \hat{r} + r \dot{\phi} \hat{\phi} \quad \text{and} \quad \dot{\vec{r}}^2 = \dot{r}^2 + r^2 \dot{\phi}^2 \quad (2.12)$$

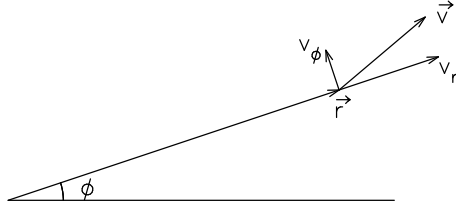


Figure 2.2: *Illustration of Eq. 2.12; $\vec{v} \equiv \dot{\vec{r}}$.*

with \hat{r} the unit vector in the direction of \vec{r} and $\hat{\phi}$ the unit vector perpendicular to \vec{r} (and in the orbital plane). For the angular momentum we obtain in these coordinates:

$$\vec{L} = r\hat{r} \times \mu \left(\dot{r}\hat{r} + r\dot{\phi}\hat{\phi} \right) = \mu r^2 \dot{\phi} \left(\hat{r} \times \hat{\phi} \right) \quad (2.13)$$

and for its scalar length:

$$L = \mu r^2 \dot{\phi} \quad (2.14)$$

The total energy of the two masses is given by the sum of the kinetic and potential energies:

$$E = \frac{1}{2} M_1 \dot{r}_1^2 + \frac{1}{2} M_2 \dot{r}_2^2 - \frac{GM_1 M_2}{r} \quad (2.15)$$

By substituting the time derivatives of \vec{r}_1 and \vec{r}_2 after Eq. 2.9 we can rewrite this as

$$E = \frac{1}{2} (M_1 + M_2) \dot{R}^2 + \frac{1}{2} \mu \dot{r}^2 - \frac{GM_1 M_2}{r} \quad (2.16)$$

Thus the total energy can be written as the kinetic energy derived from the motion of the center of mass, and the kinetic and potential energy in the relative orbit.

2.2 The relative orbit

To solve the relative orbit, we first write down the energy and angular momentum of the relative orbit per unit of reduced mass:

$$\epsilon \equiv \frac{E_{\text{bin}}}{\mu} \equiv \frac{1}{2} (\dot{r}^2 + r^2 \dot{\phi}^2) - \frac{G(M_1 + M_2)}{r} \quad (2.17)$$

$$l \equiv \frac{L}{\mu} = r^2 \dot{\phi} \quad (2.18)$$

Both ϵ and l are constants of motion. We now use Eq. 2.18 to eliminate $\dot{\phi}$ from Eq. 2.17, and find

$$\epsilon = \frac{1}{2} \dot{r}^2 - \frac{G(M_1 + M_2)}{r} + \frac{1}{2} \frac{l^2}{r^2} \quad (2.19)$$

We first investigate this equation qualitatively by defining an effective potential

$$\epsilon = \frac{1}{2} \dot{r}^2 + V_{\text{eff}} \quad \text{where} \quad V_{\text{eff}} \equiv -\frac{G(M_1 + M_2)}{r} + \frac{1}{2} \frac{l^2}{r^2} \quad (2.20)$$

The effective potential depends on the angular momentum l . Depending on the total energy ϵ we can have various types of orbits (see Figure 2.3).

1) $\epsilon > 0$: the particle moves from $r = \infty$ to a minimal distance, and back out again.

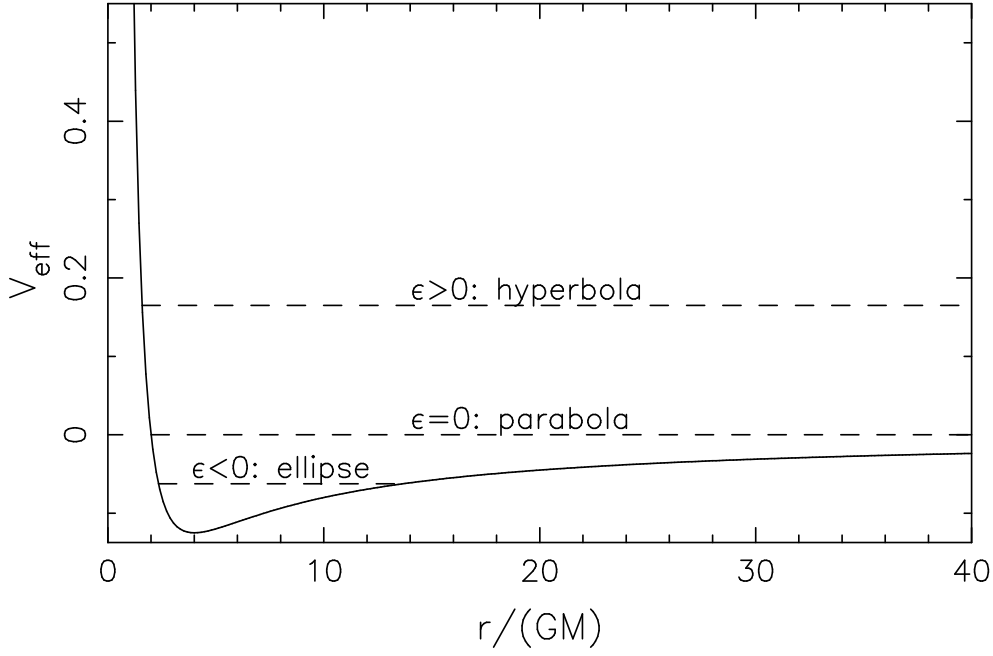


Figure 2.3: Possible orbits; the values are for $l = 2GM$ where $M \equiv M_1 + M_2$

It has a finite radial velocity \dot{r} at $r = \infty$.

- 2) $\epsilon = 0$: idem, with radial velocity equal to zero at $r = \infty$.
- 3) $\epsilon < 0$: the orbit is bound, between r_{min} and r_{max}

At the minimum of $V_{\text{eff}}(r)$, which may be found from $\partial V_{\text{eff}}/\partial r = 0$, the orbit is circular. Thus, for each given angular momentum l , the circular orbit is the orbit with the smallest total energy. No matter how small the angular momentum l is, a circular orbit is always possible. Another property of the classical solution is: the larger the energy, the closer to the origin the particle can come, but it can never ever reach the origin, as long as $l > 0$.

To solve the orbit analytically, we write r as a function of ϕ :

$$\frac{dr}{d\phi} = \frac{\dot{r}}{\dot{\phi}} = \frac{r^2}{l} \left(2\epsilon + \frac{2G(M_1 + M_2)}{r} - \frac{l^2}{r^2} \right)^{1/2} \quad (2.21)$$

Next, we substitute $u = 1/r$ to find

$$\left(\frac{du}{d\phi} \right)^2 = \frac{1}{l^2} (2\epsilon + 2G(M_1 + M_2)u - l^2u^2) \quad (2.22)$$

the solution of which is given by

$$u = \frac{1}{r} = \frac{1}{p} (1 + e \cos[\phi - \phi_o]) \equiv \frac{1}{p} (1 + e \cos \nu) \quad (2.23)$$

with

$$\frac{1}{p} = \frac{G(M_1 + M_2)}{l^2} \quad \text{and} \quad 2\epsilon = \frac{[G(M_1 + M_2)]^2}{l^2} (e^2 - 1) \quad (2.24)$$

(verify! by entering the solution in Eq. 2.22). Here ϕ_o is an integration constant; we will see below that it corresponds to periastron. Because ϕ_o is constant, we have $\dot{\nu} = \dot{\phi}$.

Eq. 2.23 is the equation for a conic section: in the Newtonian description of gravity, the relative orbit of a two masses in their mutual gravitational fields is always a conic section.

2.2.1 Some properties of elliptic motion

We will now show that, in the case of a bound orbit, when $\epsilon < 0$, the orbit corresponds to an ellipse, with eccentricity $e < 1$. The shortest distance, periastron, is reached for $\nu = 0$ at $r = p/(1 + e)$, and the longest distance, apastron, for $\nu = \pi$ at $r = p/(1 - e)$. The sum of the periastron and apastron distances is the major axis of the ellipse, $2a$, and from this we find $p = a(1 - e^2)$. p is called the semi-latus rectum, a the semi-major axis of the ellipse. Entering this result in Eqs. 2.24 and 2.23 we obtain

$$l^2 = G(M_1 + M_2)a(1 - e^2) \quad \text{and} \quad \epsilon = -\frac{G(M_1 + M_2)}{2a} \quad (2.25)$$

and

$$r = \frac{a(1 - e^2)}{1 + e \cos \nu} \quad (2.26)$$

We write the relative velocity as $v^2 \equiv \dot{r}^2 + r^2\dot{\phi}^2$. We combine Eqs. 2.17 and 2.25, noting that the total orbital energy ϵ is constant, to find

$$v^2 = G(M_1 + M_2) \left(\frac{2}{r} - \frac{1}{a} \right) \quad (2.27)$$

For peri- and apastron we get

$$r_p = a(1 - e) \quad \text{and} \quad r_a = a(1 + e) \quad (2.28)$$

Hence with Eq. 2.27 the velocities v_p and v_a at peri- and apastron are

$$v_p = \sqrt{\frac{G(M_1 + M_2)}{a} \frac{1 + e}{1 - e}}; \quad v_a = \sqrt{\frac{G(M_1 + M_2)}{a} \frac{1 - e}{1 + e}} \quad (2.29)$$

(These velocities can also be derived directly by comparing the energy Eq. 2.17 and angular momentum Eq. 2.18 at peri- and apastron.)

Now draw a coordinate system with the origin (C in Fig. 2.4) in the middle of the major axis of the ellipse, with the X -axis along the major axis, and the Y -axis along the minor axis. In this coordinate system we have from Eq. 2.26 and 2.28:

$$X = ea + \frac{a(1 - e^2) \cos \nu}{1 + e \cos \nu} = \frac{a(e + \cos \nu)}{1 + e \cos \nu} \quad \text{and} \quad Y = \frac{a(1 - e^2) \sin \nu}{1 + e \cos \nu} \quad (2.30)$$

For $X = 0$ we have $\cos \nu = -e$, and entering this in the equation for Y , we find the minor axis b :

$$b = a(1 - e^2)^{1/2} \quad (2.31)$$

With these results it is now easily shown that

$$\left(\frac{X}{a} \right)^2 + \left(\frac{Y}{b} \right)^2 = 1 \quad (2.32)$$

i.e. the relative orbit is an ellipse.

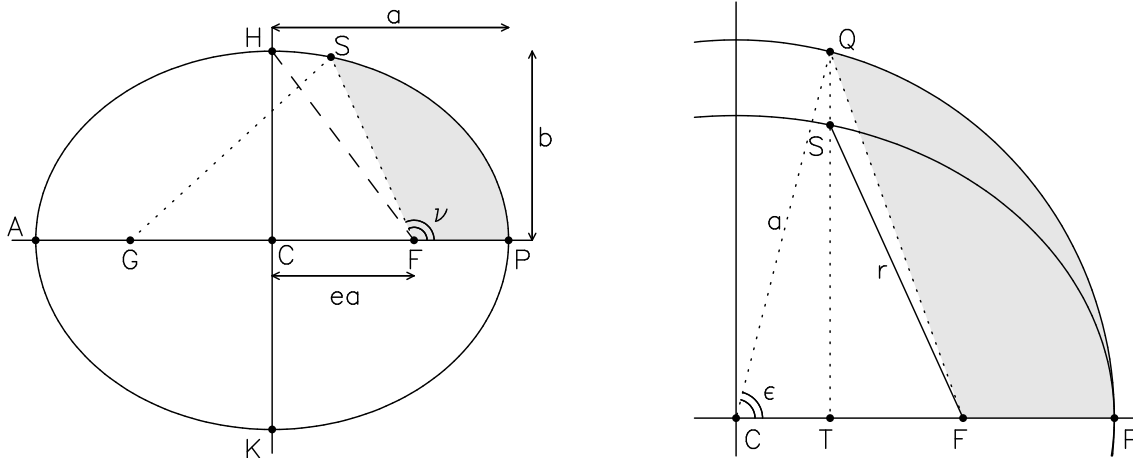


Figure 2.4: *Left: Drawings of ellipse with center C , focus F , periastron P , and apastron A . Right: Detail to illustrate derivation of equation of Kepler (Eq. 2.36).*

2.2.2 The equation of Kepler

Having established the form of the orbit $r(\nu)$, we wish to know the position as a function of time $r(t)$.

We start by deriving the second law of Kepler, that the radius vector \vec{r} covers equal area in equal times. Consider an infinitesimal time interval Δt . The area ΔO covered in this interval is $\Delta O = (1/2)|\vec{r} \times \dot{\vec{r}}\Delta t|$. Thus

$$\frac{dO}{dt} = \frac{1}{2}|\vec{r} \times \dot{\vec{r}}| = \frac{1}{2}|\vec{r} \times (\dot{r}\hat{r} + r\dot{\phi}\hat{\phi})| = \frac{l}{2} \equiv \frac{L}{2\mu} = \text{constant} \quad (2.33)$$

This is the second law of Kepler, also called the law of equal areas. By integrating we find that the area covered increases linearly with time:

$$O(t) = O(0) + \frac{L}{2\mu}t \quad (2.34)$$

We define in Figure 2.4 semi-major axis $AC=CP=a$, and semi-minor axis $HC=CK=b$. The foci of the ellipse are F at $X = ea$ and G at $X = -ea$. The periastron P has a distance to the focus F given by $PF \equiv r_p = (1 - e)a$; the apastron A has a distance to focus F given by $AF \equiv r_a = (1 + e)a$. If we have a point S on the ellipse, then the sum of the distances of this point to the foci is $GS + SF = 2a$.

The motion of the point S along the ellipse in a Kepler orbit is such that the area covered by FS , the area FPS shaded grey in Fig. 2.4 left, increases linearly with time, according to Eq. 2.34. We add to the ellipse a circle around the center C with radius a (Figure 2.4 right), and note from Eq. 2.32 that this circle can be found from the ellipse X, Y by multiplying for each X the corresponding Y value with a/b . Draw a line perpendicular to the semi-major axis through S , and call the point where this line cuts the semi-major axis T and where it cuts the circle Q . Then $QC = a$ and $QT/ST = a/b$. The area FPQ in the circle (indicated grey in Fig. 2.4 right) is a/b times the area FPS in the ellipse (indicated grey in Fig. 2.4 left), and thus also increases linearly with time. We write this as:

$$\frac{M}{2\pi} \equiv \frac{\text{Area}(FPS)}{\text{Area}(\text{ellipse})} = \frac{\text{Area}(FPQ)}{\text{Area}(\text{circle})} = \frac{\text{Area}(CPQ) - \text{Area}(CFQ)}{\pi a^2} \quad (2.35)$$

where M increases linearly with time. Now write angle QCF as ε . The area of the circle sector is $\text{Area}(\text{CPQ}) = 0.5\varepsilon a^2$. With $\text{QC} = a$ we have $\text{QT} = a \sin \varepsilon$, and the area of triangle $\text{CFQ} = 0.5\text{CF} \times \text{QT} = 0.5ae \times a \sin \varepsilon = 0.5a^2e \sin \varepsilon$. The last equality of Eq. 2.35 can then be written:

$$\frac{M}{2\pi} = \frac{0.5\varepsilon a^2 - 0.5a^2e \sin \varepsilon}{\pi a^2} \Rightarrow M = \varepsilon - e \sin \varepsilon \quad (2.36)$$

This is Kepler's equation. M is called the mean anomaly, and ε the eccentric anomaly. To express $r \equiv \text{FS}$ in terms of ε we note that $\text{ST} = (b/a)\text{QT} = b \sin \varepsilon$, thus $\text{ST}^2 = b^2 \sin^2 \varepsilon = a^2(1 - e^2) \sin^2 \varepsilon$ where we use Eq. 2.31, and therefore

$$r^2 \equiv \text{FS}^2 = \text{ST}^2 + \text{TF}^2 = \text{ST}^2 + (\text{CF} - \text{CT})^2 = a^2(1 - e \cos \varepsilon)^2 \quad (2.37)$$

hence

$$r = a(1 - e \cos \varepsilon) \quad (2.38)$$

To express ν as a function of ε we combine Eqs. 2.26 and 2.38 into

$$1 - e \cos \varepsilon = \frac{1 - e^2}{1 + e \cos \nu} \Rightarrow \tan \frac{\nu}{2} = \sqrt{\frac{1+e}{1-e}} \tan \frac{\varepsilon}{2} \quad (2.39)$$

(Since the derivation of the right hand side equation is somewhat convoluted we give the steps explicitly: From the left equation, we have

$$\cos \nu = \frac{\cos \varepsilon - e}{1 - e \cos \varepsilon} \quad \text{hence} \quad \sin \nu = \frac{\sqrt{1 - e^2} \sin \varepsilon}{1 - e \cos \varepsilon} \quad (2.40)$$

Thus, with Eq. 2.50,

$$\tan \frac{\nu}{2} = \sqrt{\frac{1 - \cos \nu}{1 + \cos \nu}} = \sqrt{\frac{(1+e)(1 - \cos \varepsilon)}{(1-e)(1 + \cos \varepsilon)}} \quad (2.41)$$

from which Eq. 2.39 follows.)

2.3 Exercises

Exercise 6. The general definition of the angular momentum is

$$\vec{L} = \int_V \rho(\vec{r} \times \vec{v}) dV \quad (2.42)$$

In the case of two point masses, this can be written

$$\vec{L} = M_1 \vec{r}_1 \times \dot{\vec{r}}_1 + M_2 \vec{r}_2 \times \dot{\vec{r}}_2 \quad (2.43)$$

Show that this can be written also as

$$\vec{L} = (M_1 + M_2) \vec{R} \times \dot{\vec{R}} + \mu \vec{r} \times \dot{\vec{r}} \quad (2.44)$$

so that the angular momentum can be split, analogously to the energy, in the angular momentum of the center of mass and the angular momentum in the binary.

Exercise 7. Start from the second law of Kepler, Eq. 2.34, to derive his third law:

$$\left(\frac{2\pi}{P}\right)^2 = \frac{G(M_1 + M_2)}{a^3} \quad (2.45)$$

Exercise 8a. Geometrical interpretation of the *semi-latus rectum*. In Figure 2.4 draw a line from the focal point F to the ellipse, perpendicular to the major axis. This line is called the semi-latus rectum. Show that its length is $a(1 - e^2)$.

b. Prove the statement that for any point S on the ellipse, the sum of the distances to the two focal points equals the major axis: $GS+SF=2a$. (Hint: write GS in terms of a , e and ε)

Exercise 9: an alternative derivation for the velocities v_p and v_a at peri- and apastron. The orbital angular momentum and the orbital energy are given by Eq. 2.25. Use the equality of energy and angular momentum at periastron with energy and angular momentum at apastron, to write two equations for v_p and v_a , and then solve for these two velocities.

Mathematical intermezzo: adding angles, half-angles

We reiterate some useful goniometric relations.

$$\begin{aligned} e^{ix} &= \cos x + i \sin x \\ e^{iy} &= \cos y + i \sin y \\ e^{i(x+y)} &= e^{ix} e^{iy} \\ \text{hence} & \end{aligned} \quad (2.46)$$

$$\cos(x + y) = \cos x \cos y - \sin x \sin y \quad (2.47)$$

$$\sin(x + y) = \cos x \sin y + \sin x \cos y \quad (2.48)$$

In the case where $x = y$ we have

$$\cos(2x) = \cos^2 x - \sin^2 x = 1 - 2 \sin^2 x = 2 \cos^2 x - 1 \quad (2.49)$$

from which we have

$$2 \sin^2 x = 1 - \cos(2x), \quad 2 \cos^2 x = 1 + \cos(2x) \Rightarrow \tan^2 x = \frac{1 - \cos(2x)}{1 + \cos(2x)} \quad (2.50)$$

Mathematical intermezzo: projection and rotation

In general, a vector \vec{r} in a plane can be written as consisting of components along the X and Y axes: $X = r \cos \phi$ and $Y = r \sin \phi$. If we wish to switch from one coordinate system X, Y to another one X_1, Y_1 , we construct a rotation matrix, as follows. Suppose the new coordinate system is at angle $-\theta$ from the previous one. We are looking for a matrix for which

$$\begin{pmatrix} X_1 \\ Y_1 \end{pmatrix} = \begin{pmatrix} R_{11} & R_{12} \\ R_{21} & R_{22} \end{pmatrix} \begin{pmatrix} X \\ Y \end{pmatrix} \quad (2.51)$$

The unit vector along the X axis is projected on the new coordinate axes as $X_1 = \cos \theta$ and $Y_1 = \sin \theta$. Therefore we take $R_{11} = \cos \theta$ and $R_{21} = \sin \theta$. The unit vector along the Y axis is projected on the new coordinate axes as $X_1 = -\sin \theta$ and $Y_1 = \cos \theta$. Therefore we take $R_{12} = -\sin \theta$ and $R_{22} = \cos \theta$. Herewith we have constructed the rotation matrix $\mathcal{R}(-\theta)$.

Consider the vector r which we want to express in a new coordinate system, rotated $-\theta$ with respect to the original system. Eq. 2.51 becomes:

$$\begin{pmatrix} r \cos \phi_1 \\ r \sin \phi_1 \end{pmatrix} = \begin{pmatrix} \cos \theta & -\sin \theta \\ \sin \theta & \cos \theta \end{pmatrix} \begin{pmatrix} r \cos \phi \\ r \sin \phi \end{pmatrix} \quad (2.52)$$

executing the multiplications, we have

$$r \cos \phi_1 = r(\cos \theta \cos \phi - \sin \theta \sin \phi) = r \cos(\theta + \phi)$$

and

$$r \sin \phi_1 = r(\sin \theta \cos \phi + \cos \theta \sin \phi) = r \sin(\theta + \phi)$$

Note that the rotation does not change the length of the vector r . Hence, perhaps not surprisingly, we see that *a rotation of $-\theta$ of the coordinate system corresponds to the addition of θ to the position angle of the original vector.*

In 3-d space, we may choose the Z -axis perpendicular to the plane we just described, and the rotation along $-\theta$ now is written as a rotation around the Z axis:

$$\mathcal{R}_z(\theta) = \begin{pmatrix} \cos \theta & -\sin \theta & 0 \\ \sin \theta & \cos \theta & 0 \\ 0 & 0 & 1 \end{pmatrix} \quad (2.53)$$

Thus, we see the close connection between projecting a vector and a rotation of the coordinate system.

Analogously, a rotation over $-\theta$ around the X -axis can be shown to be given in 3-d coordinates by:

$$\mathcal{R}_x(-\theta) = \begin{pmatrix} 1 & 0 & 0 \\ 0 & \cos \theta & -\sin \theta \\ 0 & \sin \theta & \cos \theta \end{pmatrix} \quad (2.54)$$

Chapter 3

Observing binaries

In this chapter we first derive the equation for the visual orbit of a binary, and briefly describe how it can be fitted. We then derive the radial velocities of the binary members, and describe how they are fitted. The visual orbit and radial velocities provide information about the masses of the stars. Eclipsing binaries allow us to obtain observational information on the radii of the stars. If the stars are spherical, the analysis of the eclipse is relatively straightforward. However, the mutual gravity of the stars leads to non-sphericity. In the last Section of this chapter we discuss the Roche geometry which describes the surfaces of stars in a binary, and briefly explain how this affects the analysis of eclipse observation. The non-sphericity of the stars also implies that their gravity deviates from the $1/r^2$ -law. The discussion of this deviation and its effect on the binary orbit are deferred to a later Chapter.

3.1 Projecting the binary orbit

Some angles involved in converting the binary orbit into the observed visual orbit are illustrated in Figure 3.1. To obtain the position of the star in the plane perpendicular to the line of sight, we perform two subsequent rotations. The angle ω is the angle between the long axis of the ellipse, and the line o which is the intersection of the orbital plane with the plane perpendicular to the line of sight. We project r onto o (the new X -axis) and l (the new Y axis). As derived in the intermezzo, this corresponds to adding ω to the position angle ν . We then rotate around o , the new X axis, over the inclination angle $-i$.

The coordinate system in the plane of the sky has o as its X -axis and m as its Y -axis. It is customary to take the X -axis towards the North, and thus we require a third rotation, over the angle Ω between o and the North-South line, to obtain the final coordinates. In Equation:

$$\begin{pmatrix} x' \\ y' \\ z' \end{pmatrix} = \mathcal{R}_z(-\Omega)\mathcal{R}_x(-i)\mathcal{R}_z(-\omega) \begin{pmatrix} r \cos \nu \\ r \sin \nu \\ 0 \end{pmatrix} =$$
$$\mathcal{R}_z(-\Omega)\mathcal{R}_x(-i) \begin{pmatrix} \cos \omega & -\sin \omega & 0 \\ \sin \omega & \cos \omega & 0 \\ 0 & 0 & 1 \end{pmatrix} \begin{pmatrix} r \cos \nu \\ r \sin \nu \\ 0 \end{pmatrix} =$$

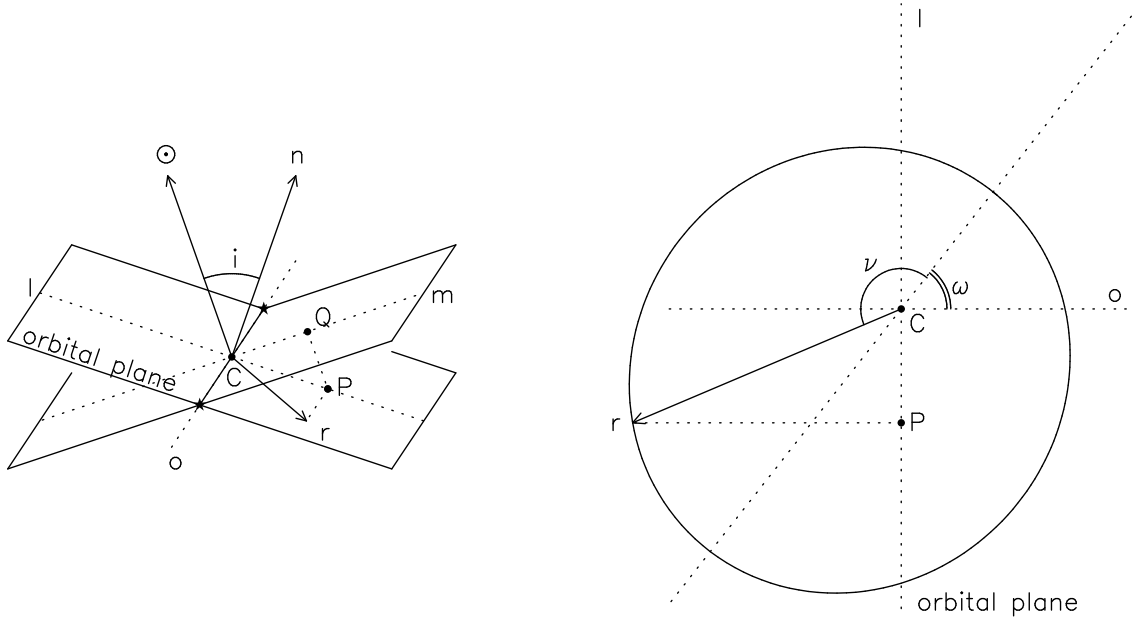


Figure 3.1: *Illustration of the planes involved in observing binary motion. C is the center around which the star moves. n is the normal to the binary plane, passing through C ; the celestial plane is drawn through C , perpendicular to the line of sight (\odot). The angle between n and \odot is the inclination i , which thus is also the angle between the two planes. l is the line through C , perpendicular to the intersection o of the two planes, in the orbital plane. m is the line through C perpendicular to the intersection, in the celestial plane. Thus, l , \odot , n and m are all in one plane, the plane through C perpendicular to the intersection. The vector r connects C with the location of the star, the projection in the orbital plane of r on l is CP , the projection of CP on m is CQ , and $PQ \equiv z$ is the distance of the star to the celestial plane. The angle between r and the semi-major axis is ν (zero at periastron), the angle between the intersection and the semimajor axis is ω .*

$$\mathcal{R}_z(-\Omega)\mathcal{R}_x(-i) \begin{pmatrix} r \cos(\omega + \nu) \\ r \sin(\omega + \nu) \\ 0 \end{pmatrix} =$$

$$\mathcal{R}_z(-\Omega) \begin{pmatrix} 1 & 0 & 0 \\ 0 & \cos i & -\sin i \\ 0 & \sin i & \cos i \end{pmatrix} \begin{pmatrix} r \cos(\omega + \nu) \\ r \sin(\omega + \nu) \\ 0 \end{pmatrix} = \mathcal{R}_z(-\Omega) \begin{pmatrix} r \cos(\omega + \nu) \\ r \sin(\omega + \nu) \cos i \\ r \sin(\omega + \nu) \sin i \end{pmatrix}$$

Computationally, it is easier to write the third rotation on the left hand side of this equation, i.e. to multiply the last equality left and right with $\mathcal{R}_z(\Omega)$. This leads to:

$$\begin{pmatrix} \cos \Omega & \sin \Omega & 0 \\ -\sin \Omega & \cos \Omega & 0 \\ 0 & 0 & 1 \end{pmatrix} \begin{pmatrix} \rho \cos \theta \\ \rho \sin \theta \\ z \end{pmatrix} = \begin{pmatrix} \rho \cos(\theta - \Omega) \\ \rho \sin(\theta - \Omega) \\ z \end{pmatrix} = \begin{pmatrix} r \cos(\omega + \nu) \\ r \sin(\omega + \nu) \cos i \\ r \sin(\omega + \nu) \sin i \end{pmatrix}$$

So finally, we can wrap up the computation, by writing the last equations as

$$x = r \cos(\omega + \nu) \tag{3.1}$$

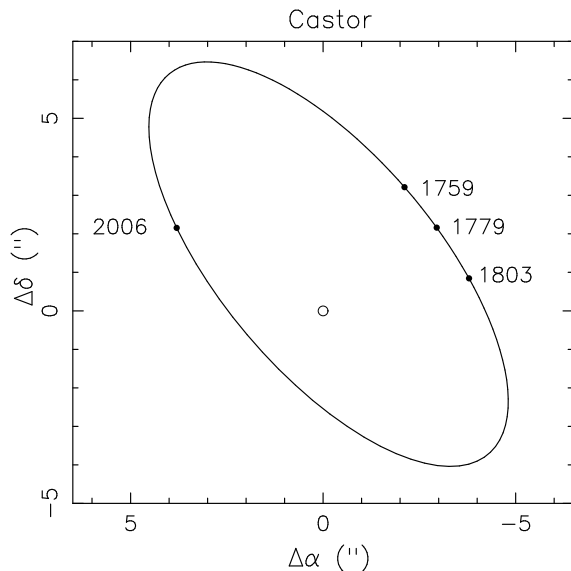


Figure 3.2: *Modern computation of the orbit of Castor B relative to Castor A. The positions in various years are indicated. Compare with Herschel’s observations in Figure 1.4.*

parameter	symbol	Castor AB
orbital period	P	467.0 yr
time of periastron passage	T	1958.0
semi-major axis	a	6.805"
eccentricity	e	0.343
inclination	i	114.5°
angle periastron/node-line	ω	249.5°
angle North/node-line	Ω	41.3°

Table 3.1: *Parameters required to describe a visual orbit, their symbols, and as an example the values for Castor (from Heintz 1988).*

$$y = r \sin(\omega + \nu) \cos i \quad (3.2)$$

$$z = r \sin(\omega + \nu) \sin i \quad (3.3)$$

$$\rho = \sqrt{x^2 + y^2} \quad (3.4)$$

$$\theta = \Omega + \text{atan} \frac{y}{x} \quad (3.5)$$

3.1.1 Computing and fitting the visual orbit

To illustrate the computation of the relative positions of two stars in a binary at time t , we compute the relative position of Castor B with respect to Castor A at the time of Herschel’s first observation. We use the orbital parameter as determined by Heintz (1988), listed in Table 3.1.

Step 1. Herschel’s first observation is from 11 May 1779. Since the period is in years, we write this as $t = 1779.36$. We compute the mean anomaly from:

$$M = \frac{2\pi}{P}(t - T) \quad (3.6)$$

and find $M = -2.403$ radians.

Step 2. We solve the eccentric anomaly ε from Kepler's equation Eq. 2.36, to find: $\varepsilon = -2.585$ radians

Step 3. We compute the radius vector in the orbital plane r and the real anomaly ν from Eqs. 2.38 and 2.39. Results: $r = 8.787''$ and $\nu = -2.747$.

Step 4. We compute the coordinates with respect to the line of nodes, in the plane of the sky, and from this the radius vector and position angle with respect to the North, from Eqs. 3.1-3.5. Results: $x = -0.324$, $y = -3.641$, $\rho = 3.656$, $\theta - \Omega = -95.08^\circ$, hence $\theta = -53.78^\circ$, equivalent to $\theta = 306.22^\circ$. The tricky thing here is to obtain $\theta - \Omega$ in the right quadrant. If one computes $\text{atan}(y/x)$, the answer is the same for x and y both negative as for x and y both positive, but the quadrant in which the result lies is not the same!

Step 5. We can now plot the relative position of the two stars. Putting Castor A at the origin, and noting that the angle θ by definition increases from the North, anti-clockwise. The relative position can be expressed in the directions of right ascension and declination, as:

$$\Delta\alpha = \rho \sin \theta \quad \text{and} \quad \Delta\delta = \rho \cos \theta \quad (3.7)$$

Note that in the figure, as on the sky, the right ascension increases towards the left.

The inverse problem from plotting a known orbit is to solve the orbital parameter from a set of observations $\Delta\alpha_i$, $\Delta\delta_i$ obtained at N times t_i . For a set of assumed values for the orbital parameters listed in Table 3.1 we can compute for each observing time t_i the model values $\Delta\alpha_m(t_i)$ and $\Delta\delta_m(t_i)$. If the measurement errors in right ascension and declination at time t_i are $\sigma_{\alpha,i}$ and $\sigma_{\delta,i}$ respectively, and if these errors are Gaussian, the quantity to be minimized is:

$$\chi^2 = \sum_{i=1}^N \left[\frac{(\Delta\alpha_i - \Delta\alpha_m(t_i))^2}{\sigma_{\alpha,i}^2} + \frac{(\Delta\delta_i - \Delta\delta_m(t_i))^2}{\sigma_{\delta,i}^2} \right] \quad (3.8)$$

In general, this minimization cannot be done directly, but must be done with successive improvements on an initial trial solution. The solution to the problem consists of 1) the best parameter values 2) the errors on the parameter values 3) the probability that the model describes the observed orbit (as given by the probability that the model would give rise to a χ^2 with the observed value or larger).

The minimization provides us with the values for the parameters listed in Table 3.1. Of these parameters, T , i , ω and Ω are not essential for the binary itself, but only indicate relations with the direction to and time measurement on Earth. Relevant parameters for the binary are the orbital period P , the eccentricity e and the semi-major axis a . From the visual orbit alone, a is only known in angular units.

If the orbits of both stars can be measured separately with respect to the sky (after correction for parallax and proper motion), then from Eq. 2.9 we see that the ratio of the semi-major axes gives the ratio of the masses: $a_1/a_2 = M_2/M_1$.

If the distance to the binary is known, for example because its parallax is measured, or because it is in a star cluster, we can compute the semi-major axis in cm, and thus from Kepler's third law Eq. 2.45 derive the total mass.

If both distance and mass ratio are known we can derive the masses M_1 and M_2 separately.

3.2 Radial velocities

From Eq. 3.3 we have the distance z of the star to the plane perpendicular to the line of sight. The derivative of z corresponds to (a component of) the radial velocity:

$$\dot{z} = \dot{r} \sin(\omega + \nu) \sin i + r \dot{\nu} \cos(\omega + \nu) \sin i$$

To rewrite this, we first use the angular momentum, as expressed in Eq. 2.18, and then rewrite it, using Eqs. 2.25 and 2.26:

$$r \dot{\nu} = r \dot{\phi} = \frac{l}{r} = \sqrt{\frac{G(M_1 + M_2)}{a(1 - e^2)}} (1 + e \cos \nu) \quad (3.9)$$

Next, we take the time derivative of Eq. 2.26 and rewrite it with Eq. 3.9:

$$\dot{r} = \frac{a(1 - e^2)}{(1 + e \cos \nu)^2} e \sin \nu \dot{\nu} = \frac{a(1 - e^2)}{(1 + e \cos \nu)^2} e \sin \nu \frac{l}{r^2} = \sqrt{\frac{G(M_1 + M_2)}{a(1 - e^2)}} e \sin \nu \quad (3.10)$$

Entering these results Eq 3.9 and 3.10 into the equation for \dot{z} , we find

$$\begin{aligned} \dot{z} &= \sqrt{\frac{G(M_1 + M_2)}{a(1 - e^2)}} \sin i [\cos(\omega + \nu) + e \cos \nu \cos(\omega + \nu) + e \sin \nu \sin(\omega + \nu)] \\ &= \sqrt{\frac{G(M_1 + M_2)}{a(1 - e^2)}} \sin i [\cos(\omega + \nu) + e \cos \omega] \equiv K [\cos(\omega + \nu) + e \cos \omega] \end{aligned} \quad (3.11)$$

where the last equality defines K .

In practice, an observed velocity does not belong to the reduced mass, but to one of the two stars. Let us for the moment consider that the star whose radial velocity is measured is labeled 1. We define

$$K_1 \equiv \frac{a_1}{a} K = \sqrt{\frac{G(M_1 + M_2)}{a^3(1 - e^2)}} a_1 \sin i \Rightarrow a_1 \sin i = \left(\frac{P}{2\pi}\right) (1 - e^2)^{1/2} K_1 \quad (3.12)$$

where we have further used that $a_1/a = M_2/(M_1 + M_2)$ (see Eq. 2.9). With K_1 we derive a useful quantity, called the *mass function* for star 1. Multiply the third law of Kepler Eq. 2.45 left and right with $(a_1 \sin i)^3/G$, and use Eq. 3.12 to find the mass function $f(M_1)$:

$$f(M_1) \equiv \frac{M_2^3 \sin^3 i}{(M_1 + M_2)^2} = \frac{P}{2\pi G} K_1^3 (1 - e^2)^{3/2} \quad (3.13)$$

From Eq. 3.11 we see that the parameters K , e and ω define the radial velocity curve. K defines the amplitude of the velocity curve, and e (through the non-linearity of ν with time) and ω (as a phase angle) define the form of the curve. In an observed binary, the motion of the center of mass must be added to the average velocity. To visualize how the average radial velocity can differ from zero, consider an eccentric binary with the major axis in the plane of the sky. There are two possibilities: the maximum velocity away from us is at periastron (or at apastron), then the maximum velocity towards us is at apastron (or at periastron), and thus the average of these two is away from us (towards us).

If both velocity amplitudes K_1 and K_2 are measured, we have the mass ratio, as can be seen from dividing the two mass functions Eq. 3.13 and its analogon for star 2: $M_1/M_2 = K_2/K_1$. We also have lower limits to each of the two masses M_1 and M_2 , from the mass functions. But further than this one cannot go.

If the inclination is known and both amplitudes then we can solve both masses separately, as well as the semi-major axis.

3.3 Computing eclipses

For the moment we assume that both binary stars are spherical. A spherically symmetric star gives the same flux no matter from which direction it is observed, provided it is not eclipsed. For this reason, it is relatively easy to compute its eclipse by a spherical companion.

Before we do this, we reiterate some basic equations that describe the flux leaving a stellar surface. We start by considering a unit surface of the star; this is sufficiently small to be considered flat. The energy flux $dF_\lambda(\theta)$ at wavelength λ leaving the surface under an angle θ with the normal to the surface is given by

$$dF_\lambda(\theta) = I_\lambda(\theta) \cos \theta d\omega = I_\lambda(\theta) \cos \theta \sin \theta d\theta d\phi \quad (3.14)$$

We obtain the flux leaving the unit surface by integrating over the spatial angle $d\omega$; due to symmetry, the integration over ϕ gives 2π , and we obtain:

$$F_\lambda = 2\pi \int_0^{\pi/2} I_\lambda(\theta) \cos \theta \sin \theta d\theta \equiv 2\pi \int_0^1 I_\lambda(\mu) \mu d\mu \quad (3.15)$$

where we have defined $\mu \equiv \cos \theta$. Integrated over the stellar surface, we obtain the (monochromatic) luminosity of the star

$$L_\lambda = 4\pi R^2 F_\lambda \quad (3.16)$$

Now consider the star from a large distance, and compute the flux f_λ through a unit surface at that distance. The light reaching us from the center of the star leaves its surface along the normal, but the light reaching us from positions away from the center leaves the star at an angle to the surface. A circle at projected distance $r = R \sin \theta$ from the star center has a projected surface $2\pi r dr = 2\pi R^2 \sin \theta \cos \theta d\theta$, and at large distance d subtends a spatial angle $d\omega = 2\pi(R/d)^2 \sin \theta \cos \theta d\theta$. The radiation from this circle leaves the stellar surface under an angle θ . From the definition of the intensity I according to Eq. 3.14, we can write the flux f_λ as

$$f_\lambda = \frac{2\pi}{d^2} \int_0^R r I_\lambda(r) dr = 2\pi \left(\frac{R}{d}\right)^2 \int_0^{\pi/2} I_\lambda(\theta) \cos \theta \sin \theta d\theta = F_\lambda \left(\frac{R}{d}\right)^2 \quad (3.17)$$

From this we see that energy is conserved as the flux travels from the stellar surface to distance d :

$$L_\lambda = 4\pi R^2 F_\lambda = 4\pi d^2 f_\lambda \quad (3.18)$$

This assumes, of course, that there is no interstellar absorption; for the moment we will continue to make this assumption.

A stellar atmosphere model provides the flux F_λ leaving a unit surface of the star. The model depends on 1) the effective temperature 2) the gravity at the

parameter	symbol
radius of star 1	R_1
effective temperature of star 1	T_1
radius of star 2	R_2
effective temperature of star 2	T_2

Table 3.2: *Parameters added to those of Table 3.1 for the study of an eclipsing binary. In principle the metallicity of both stars should be added; however, this are usually determined not from the eclipses, but from the out-of-eclipse spectra.*

stellar surface $g \equiv GM/R^2$, usually expressed as $\log g$ 3) the abundances of the elements. If the whole star is observed, this is sufficient for a description of the stellar spectrum. When part of the surface is blocked, as in an eclipse, we need the intensity $I_\lambda(\theta)$ as a function of angle with the normal. These intensities are also provided by a stellar atmosphere model. The drop of intensity with angle θ is called limb-darkening, and is caused by the fact that the radiation leaving the star at a large angle originates in a region closer to the stellar surface, and therefore cooler than the deeper layer which produces the radiation leaving the stellar surface along the normal. It is best to use these intensities, tabulated as a function of θ ; but when these are not available (as in many old studies), one can take recourse to an approximate formula. Often an equation was used of the form

$$I_\lambda(\mu) = I_\lambda(1) (a_0 + a_1\mu) \quad (3.19)$$

or higher order approximations. The constants a_0 and a_1 in general may depend on wavelength. For quick estimates one may use the Eddington approximation, which has $a_0 = 2/5$ and $a_1 = 3/5$. The normalization $I_\lambda(1)$ must be chosen to give the correct flux F_λ with Eq. 3.15.

With this background we are ready to compute the eclipse lightcurve. In addition to the orbital parameters listed in Table 3.1 we now have the parameters listed in Table 3.2

To compute a lightcurve, one first divides the orbit into a number of time intervals. For each time, one proceeds as follows.

Step 1. Compute the projected distance ρ between the two stars, just as in the case of the visual binary, with the parameters of Table 3.1.

Step 2. Check, with the parameters from Table 3.2, whether $R_1 + R_2 > \rho$. If not, both stars are seen in full, and the total flux is the sum of the fluxes of the two stars. If $R_1 + R_2 < \rho$ the eclipse is in progress, and we must continue.

As an example, Figure 3.3 show the apparent orbit on the sky of a recently discovered eclipsing brown dwarf, and also the projected distance between the stars as a function of time.

Step 3. Give the eclipsed star index 1, and the eclipser index 2. Compute for each $r = R_1 \sin \theta$ which fraction of the ring at r is covered. Some rings (e.g. those with $r < \rho - R_2$) are wholly visible, others are wholly covered, as illustrated in Figure 3.4. (For details, see Section 3.3.2.)

Step 4. Finally, integrate $I_\lambda(\mu)$ over the visible part of the star. (Alternatively, integrate $I_\lambda(\mu)$ over the eclipsed part, and subtract the result from the out-of-eclipse flux.) The intensity $I_\lambda(\mu)$ is found by looking up the appropriate stellar atmosphere model, characterized by T_1 and $\log g_1 = \log(GM_1/R_1^2)$. The integral can be done by dividing the stellar surface in a finite number of (projected) surface rings.

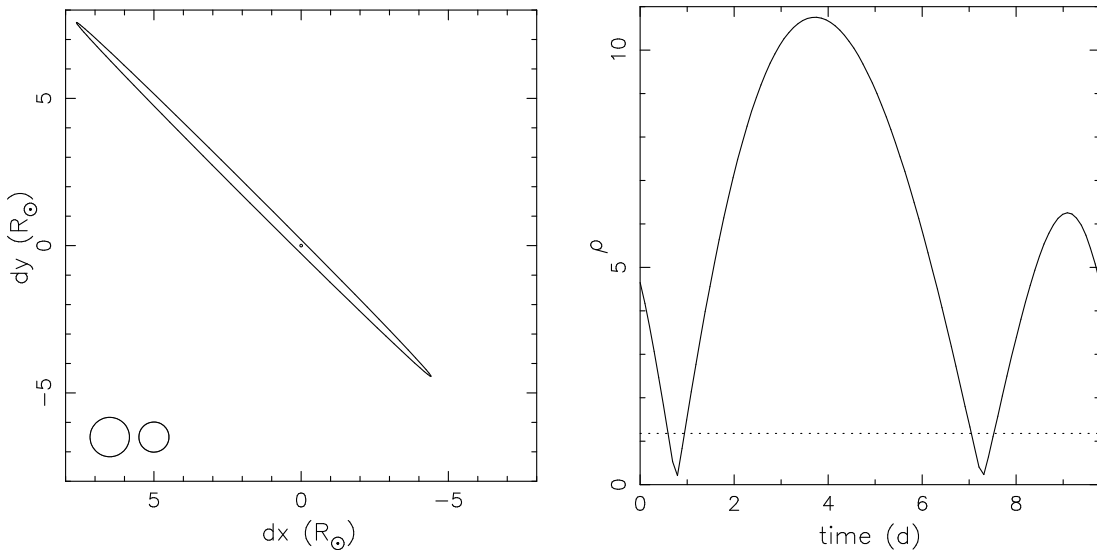


Figure 3.3: *Left: apparent orbit on the sky of the binary brown dwarf 2M J05352184–0546085 as determined from the radial velocities and eclipse; note that the angle with North is arbitrarily chosen. In the left-low corner the sizes of the two stars are indicated. Right: projected distance ρ between the centers of the stars as a function of time. The sum of the radii of both stars is indicated as a horizontal dotted line. The eclipses occur where $\rho < R_1 + R_2$. (See Stassun et al. 2007)*

The effect of limb-darkening is to make the eclipse narrower: at the beginning of the eclipse (called ingress) and at the end (egress), the change in flux is less for a limb-darkened atmosphere, and when the center of the star is eclipsed the variation is stronger in a limb-darkened atmosphere.

In fitting lightcurves, one most often uses data from many orbits, which are averaged into an average lightcurve. This implies that the orbital period is found from a separate analysis, and known before the eclipse lightcurves are fitted. Thus, the separation where the eclipse begins (or ends) directly gives the sum of the two radii, in units of the semi-major axis. Note that the radii of the stars scale with the distance, so that $R_{1,2}$ are only known in angular size, i.e. as $R_{1,2}/d$. The fluxes of both stars, as observed on earth, scale with $(R_{1,2}/d)^2$. This implies that the solution of the lightcurve can only deliver the stellar radii in angular units. The only place where the stellar masses enter are in the choice of $\log g$ for the stellar atmosphere model; this choice also is best made on the basis of the analysis of the out-of-eclipse spectrum, and is usually not very sensitive to the stellar mass.

3.3.1 Uniform disk

We first consider the case of constant intensity $I_\lambda(\theta) = I_\lambda = \text{constant}$. From Eq. 3.15 we find the flux at the surface

$$F_\lambda = \pi I_\lambda \quad (3.20)$$

and from Eq. 3.17 the flux observed at distance d

$$f_\lambda = 2\pi \left(\frac{R}{d}\right)^2 I_\lambda(\theta) \int_0^{\pi/2} \cos \theta \sin \theta d\theta = \pi I_\lambda \left(\frac{R}{d}\right)^2 \quad (3.21)$$

The latter equation could also have been derived by combining Eqs.3.20 and 3.16.

The uniform disk assumption is often made in conjunction with the assumption that the emitted spectrum is given by the Planck function:

$$B_\lambda d\lambda = \frac{2\pi hc^2}{\lambda^5} \frac{1}{e^{hc/\lambda kT} - 1} d\lambda \equiv \frac{C_1}{e^{C_2/T} - 1} \quad (3.22)$$

where

$$C_1 = 1.10 \cdot 10^6 \left(\frac{806 \text{ nm}}{\lambda} \right)^5 \text{ watt m}^{-2} \text{ nm}^{-1}; \quad C_2 = \frac{806 \text{ nm}}{\lambda} 17850.8 \text{ K} \quad (3.23)$$

Note that 806 nm is the effective wavelength of the I filter.

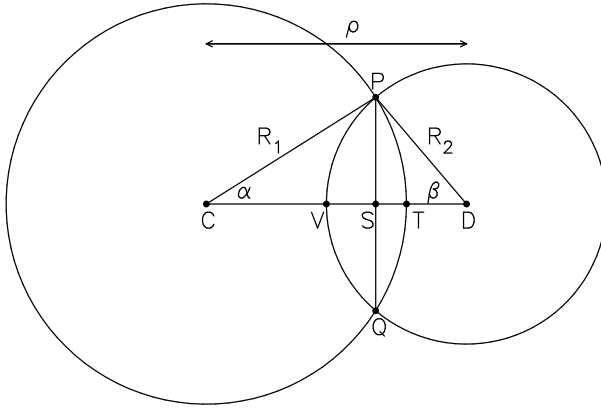


Illustration of the computation of the eclipsed area when a star with radius R_1 covers part of the star with radius R_2 , for distance ρ between the centers.

Now consider two stars, with radii R_1, R_2 and uniform intensities $I_{\lambda 1}, I_{\lambda 2}$. Away from the eclipse, when the projected distance ρ between the stars exceeds the sum of the radii, the flux observed at distance d is

$$f_\lambda = \pi I_{\lambda 1} \left(\frac{R_1}{d} \right)^2 + \pi I_{\lambda 2} \left(\frac{R_2}{d} \right)^2 \quad (3.24)$$

We first consider the case where star 1 eclipses part of star 2, i.e. the circles outlining both stars intersect in two points (P and Q in Figure 3.3.1). The flux observed from star 2 is diminished by the eclipsed lenticular surface PVQT; the flux of star 1 is not affected. The intersection points P,Q are connected by a line which is a chord in both circles, subtended by angles 2α (from center of star 1) and 2β (from center of star 2) given by the cosine-rule as:

$$A \equiv \cos \alpha = \frac{\rho^2 + R_1^2 - R_2^2}{2\rho R_1} \quad B \equiv \cos \beta = \frac{\rho^2 + R_2^2 - R_1^2}{2\rho R_2} \quad (3.25)$$

To compute the eclipsed area we first consider the right hand side of the lenticular surface, i.e. area PSQT, and in particular the upper half PST. The area of PST may be computed by subtracting triangle CSP from the circle sector CTP. The area of the triangle is $0.5R_1^2 \cos \alpha \sin \alpha$, the area of the sector $\alpha/(2\pi)$ times the area πR_1^2 of the projected area of star 1. Therefore the right hand part of the lenticular area is given by

$$\text{PSQT} = 2\text{PST} = (\alpha - \sin \alpha \cos \alpha)R_1^2 \quad (3.26)$$

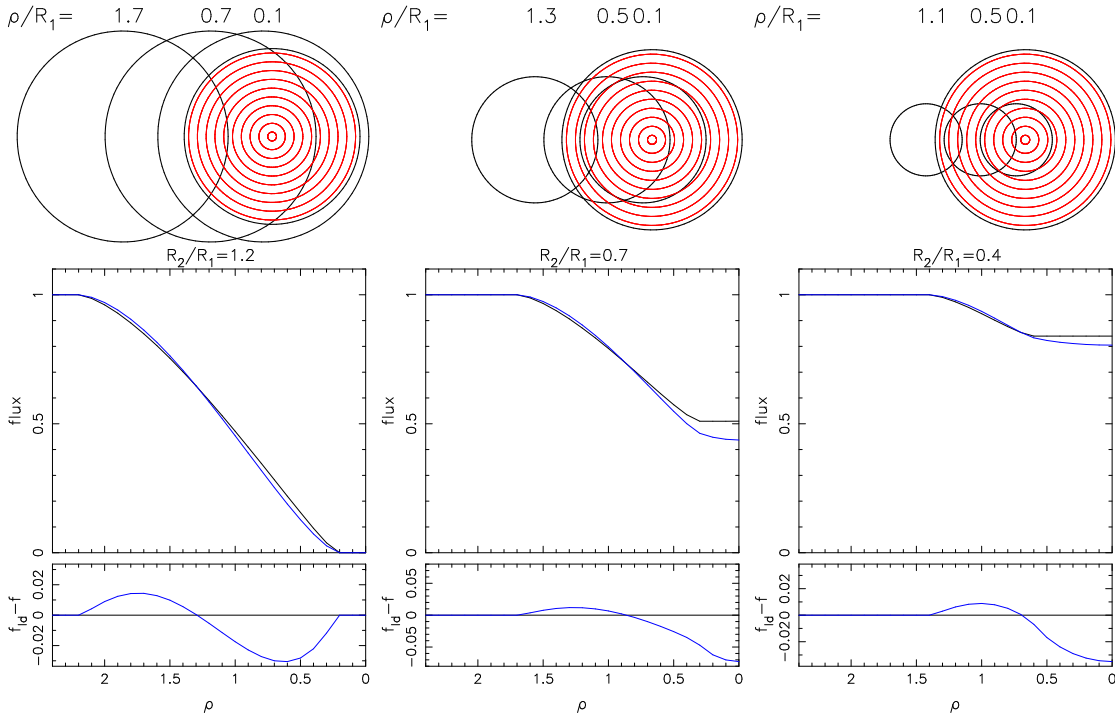


Figure 3.4: *Various eclipse geometries and fluxes. For three ratios of stellar radii R_2/R_1 , where R_1 is the eclipsed star, the top graphs illustrate the geometry, and the lower graphs the non-eclipsed flux. The fluxes are computed for a homogenous circle (f , for $I = \text{constant}$), and for a sphere with Eddington limb darkening (f_{ld}). The latter are shown in blue, and the difference with the homogeneous circle, $f_{\text{ld}} - f$, is also shown. Note that the fluxes are plotted as a function of distance between the stars, NOT as a function of time.*

Analogously we find for the left hand part

$$\text{PSQV} = 2\text{PSV} = (\beta - \sin \beta \cos \beta) R_2^2 \quad (3.27)$$

Finally we express the eclipsed full lenticular area as a fraction of the projected surface of star 2, πR_2^2 ,

$$w \equiv \frac{\text{PVQT}}{\pi R_2^2} = \frac{\arccos(A) - A\sqrt{1-A^2}}{\pi} \left(\frac{R_1}{R_2}\right)^2 + \frac{\arccos(B) - B\sqrt{1-B^2}}{\pi} \quad (3.28)$$

and obtain the flux during partial eclipse of star 2 as

$$f_\lambda = \pi I_{\lambda 1} \left(\frac{R_1}{d}\right)^2 + (1-w)\pi I_{\lambda 2} \left(\frac{R_2}{d}\right)^2 \quad (3.29)$$

When there is no intersection between the outlines of the stars, even though $\rho < R_1 + R_2$, there are two possibilities: star 2 is wholly covered ($w = 1$) if $R_1 > R_2$, or maximally covered with $w = (R_1/R_2)^2$ if $R_1 < R_2$.

3.3.2 Eclipse of limb-darkened star

Eq. 3.17 suggests that the integral is most easily computed after conversion to coordinate μ . However, for an eclipse we do need the radius in the computation of the

eclipsed fraction, and also prefer a more uniform coverage in r rather than in μ . We therefore define $x \equiv r/R$ to rewrite Eq. 3.17 as

$$f_\lambda = \frac{1}{d^2} \int_0^R 2\pi r I_\lambda(r) dr = \frac{2\pi R^2}{d^2} \int_0^1 x I_\lambda(x) dx$$

With the definition $\Xi \equiv xI(x)$, the integral can be written as a sum over rings with constant r :

$$f_\lambda = \frac{2\pi R^2}{d^2} \Delta x \sum_i x_i I_\lambda(x_i) \equiv \frac{2\pi R^2}{d^2} \Delta x \sum_i \Xi_i \quad (3.30)$$

An eclipse is in progress for each phase at which $\rho < R_1 + R_2$. For each such ρ , we compute the arccos of the eclipsed angle ϕ for each ring r as by first computing

$$z \equiv \cos(\phi) = \frac{r^2 + \rho^2 - R_1^2}{2\rho r}$$

If $-1 < z < 1$, we can indeed compute $\phi = \arccos(z)$, and the eclipsed fraction of the ring; the fractions covered are given by ϕ/π . If $|z| > 1$ the ring does not intersect the outline of the eclipsing star 2, with radius R_2 , which means that it is either fully eclipsed, or not eclipsed at all (see Fig. 3.4). The eclipsed flux is then computed from

$$f_{\lambda,e} = \frac{2R^2}{d^2} \Delta x \sum_i \phi_i \Xi_i$$

and the observed flux from

$$f_{\lambda,o} = f_\lambda - f_{\lambda,e}$$

The (monochromatic) luminosities of both stars scale with the square of the distance of the binary, and often the uncertainty in the luminosities is dominated by the distance uncertainty. In that case, the *ratio* of the luminosities may be more accurate than either luminosity separately.

3.4 Roche geometry and the Von Zeipel theorem

A star no longer is spherical when it is rotating and/or when it feels the gravity of another star. This deviation of spherical symmetry has an effect at various points in the study of binaries. We briefly investigate the deformation of and limit to the stellar surface due to the presence of a companion star, and the effect of the deformation on the eclipse and on the radial velocity curve, which requires an adapted method of fitting observations of a binary when deformations are important (Chapter 3.4.1). Some other processes that affect the lightcurve are briefly mentioned also (Chapter 3.4.2).

The potential in a binary is determined by the gravitational attraction of the two stars, and by the motion of the two stars around one another. For simplicity, we assume that the potential of each star separately, can still be written as that of a point source; and we discuss a binary with a circular orbit. In the binary frame, one has

$$\Phi = -\frac{GM_1}{r_1} - \frac{GM_2}{r_2} - \frac{\omega^2 r_3^2}{2} \quad (3.31)$$

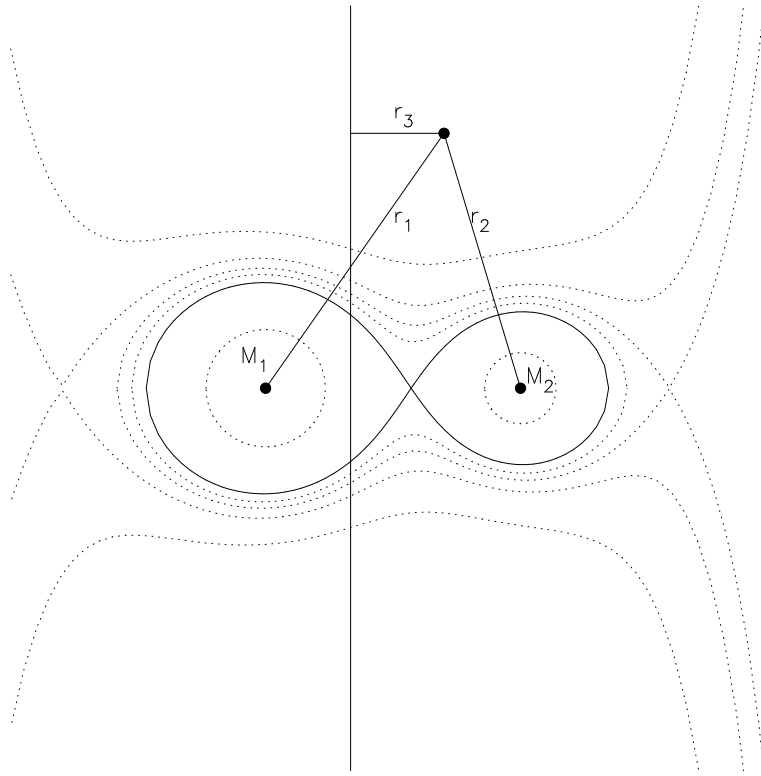


Figure 3.5: *Roche lobe geometry for a mass ratio $M_1/M_2 = 2$. Equipotential surfaces are shown for different values of $-\Phi = C$. For the largest value of C the surface consist of two separate lobes, one around each star. The Roche lobe is the surface around both stars that passes through the inner Lagrangian point. Also shown are the surfaces containing the two outer Lagrangian points. The vertical line is the rotation axis.*

where r_1 and r_2 are the distances to the center of the stars with mass M_1 and M_2 , respectively; ω is the orbital angular velocity, given by

$$\omega \equiv \frac{2\pi}{P_b} = \sqrt{\frac{G(M_1 + M_2)}{a^3}} \quad (3.32)$$

and r_3 is the distance to the axis of rotation of the binary (see Figure 3.5). Writing Eq. 3.31 in dimensionless units (mass in units of the total mass, and distances in units of the semi-major axis a), one sees that the form of the surfaces of constant Φ depends only on the mass ratio M_1/M_2 .

We can discriminate four types of surfaces of $-\Phi = C$, with C a positive constant. For large C , the potential surface consists of two closed surfaces, one around each star. For a critical value of C , the two closed surfaces touch, in the inner Lagrangian point. The surface at this value of C is called the Roche lobe (see Roche 1859). For smaller values of C we have a closed surface around both stars, and for very small values the surfaces become open.

The volume of the Roche lobe can be calculated numerically. A useful approximate formulae for the average radius of the Roche lobe around the most massive star (with mass M_1) is:

$$\frac{R_L(M_1)}{a} \simeq 0.38 + 0.2 \log \frac{M_1}{M_2} \quad (3.33)$$

which is accurate to 2 % for mass ratios $0.2 < M_1/M_2 < 20$. For the average radius of the Roche lobe around the less massive star, with mass M_2 , one may use the approximate formula:

$$\frac{R_L(M_2)}{a} \simeq 0.46 \left(\frac{M_2}{M_1 + M_2} \right)^{1/3} \quad (3.34)$$

which is accurate to 2 % for mass ratios $M_2/M_1 < 0.8$. An approximate equation valid for all mass ratios is

$$R_{L1} = \frac{0.49a}{0.6 + q^{-2/3} \ln(1 + q^{1/3})} \quad \text{where} \quad q \equiv \frac{M_1}{M_2} \quad (3.35)$$

A particle within the Roche lobe is attached to one star; a particle on the Roche lobe can move to the other star. Thus, if a star reaches the size of the Roche lobe, mass transfer may ensue. This can occur because the star expands in the course of its evolution, or because the binary shrinks. An evolving star in a binary can fill its Roche lobe for the first time as it expands on the main sequence (Case A), as it expands after hydrogen exhaustion (Case B), or as it expands after helium exhaustion (Case C). Which of the three cases applies, depends on the size of the Roche lobe, which in turn depends on the distance between the two stars and (to a lesser extent) on the mass ratio (see Eqs. 3.33-3.35).

If a star has a deformed, but stationary structure, hydrostatic equilibrium still holds: the gradient of the pressure P is balanced by the gravitational force, which can be written as the derivative of the gravitational potential Φ :

$$\nabla P = -\rho \nabla \Phi \quad (3.36)$$

Thus, the gradient of the pressure is everywhere parallel with the gradient of the potential: this implies that surfaces of constant potential are also surfaces of constant pressure $P = P(\Phi)$. In Eq. 3.36, we then find that ρ is a function of the potential only, since it depends only on $P(\Phi)$ and Φ . Thus, equipotential surfaces also have a constant density $\rho = \rho(\Phi)$, and via the equation of state also a constant temperature $T = T(\Phi)$.

The equation of radiative transport is:

$$\nabla T = -\frac{3\kappa\rho}{4\sigma} \frac{1}{4T^3} F_{\text{rad}} \quad (3.37)$$

where κ is the opacity, σ the Stefan-Boltzmann constant, and F_{rad} the radiative flux. In a deformed star, the distances between equipotential surfaces are different in different directions. Since equipotential surfaces have a constant temperature, the temperature derivative must also be different in different directions: smaller (larger) when the equipotential surfaces are further apart (closer). With Eq. 3.37 we find that the flux across an equipotential surface, and thus the flux at the stellar surface, varies. This is called the Von Zeipel theorem (see Von Zeipel 1924). This theorem was first used in the context of rapidly rotating single stars, to show that the effective temperatures at the equator are lower than at the poles. Similarly in a binary, a star that fills its Roche lobe has a lower effective temperature near the inner Lagrangian point. This effect is called *gravity darkening*.

3.4.1 Fitting binary observations in Roche geometry

When a star in a binary is deformed from a sphere, its eclipses will look different, for two reasons:

- the geometry of the eclipse is different
- the temperature, and therefore the flux and the spectrum, varies over the stellar surface, due to the Von Zeipel theorem

The center of light of the deformed star no longer necessarily coincides with the center of mass. This implies that the radial velocity measurements are also affected. Also, the strength of a spectral line depends on the temperature and the gravity, and therefore varies over the surface of a deformed star. This also tends to displace the measured velocity from the velocity of the center of mass of the star.

To really compute these effects, one would require a three-dimensional model of the stellar interior. In the absence of such models, various simplifications are made, of which the most important is the assumption that the effective temperature T_e of a stellar surface element scales with the gradient of the potential there according to

$$\frac{T_e}{T_{e,pole}} = \left(\frac{F}{F_{pole}} \right)^{0.25} = \left(\frac{\nabla\Phi}{\nabla\Phi_{pole}} \right)^g \quad (3.38)$$

where $F \equiv \sigma T_e^4$ is the energy flux leaving the surface. The exponent g depends on the type of star, and has the value $g = 0.25$, that follows from simple application of the Von Zeipel theorem Eq. 3.37 for a star with a radiative envelope. For stars with a convective envelope, the value of g is lower, $g = 0.08$.

By integrating F_e over the stellar surface, and equating the result with the stellar luminosity, one finds the normalization constant $F_{e,pole}$.

It is then straightforward, but computationally expensive, to compute a lightcurve. First compute the form of the surface of each star, which is an equipotential surface, characterized by Eq. 3.31 with a constant Φ . For the sake of computation, this surface is divided in small elements. Next assign each surface element of the star a spectrum with the appropriate effective temperature and gravity, and then compute for each viewing angle which surface elements are visible, and add their contributions to the flux, or for the spectrum to the flux distributions taking into account the Doppler shift due to the velocity of the surface element with respect to the observer. Thus computing the flux and radial velocity at each orbital phase one may compare to the observations, and where necessary adapt the binary parameters to improve the fit.

The main effect of the deformation of a star into a pear shape is the *ellipsoidal variation*. At conjunction of the two stars, we see smaller areas than when the stars are in the plane of the sky. Thus the flux observed from the binary varies throughout the orbit, with two minima each orbit at conjunction, and two maxima in between. Figure 1.5 shows several examples, and also illustrates that the amplitude of the ellipsoidal variation is larger when a star is closer to filling its Roche lobe, i.e. when it is more deformed. Obviously, the amplitude of the variation also depends on the inclination, being largest at $i = 90^\circ$.

The first widely used code to fit a binary lightcurve is that of Wilson & Devinney (1971). This early version still had many simplifications. In particular it described

the radiation emitted by each surface element as a black body, only applying colour corrections (from black body to stellar atmosphere spectrum) to the integrated flux. In the course of time, as computers became faster, the code has been improved. An example of a modern version is given by Orosz & Hauschildt (2000). The latter code takes into account the effects of *limb darkening* (see discussion near Eq. 3.19). These codes find the best solution by minimizing a optimization function, in particular the χ^2 function.

It is impossible to find the best parameters of the binary reliably by using a standard routine for this minimization as the Levenbergh-Marquardt routine (described in e.g. *Numerical Recipes*, Chapter 15.5, Press et al. 1992), because the number of parameters is too large. Orosz has therefore experimented with another method, the *genetic algorithm* which cleverly uses random numbers to search the parameter space for the best solution, and this works very well. An very clear description of the genetic algorithm and its applications is given by Charbonneau (1995R; in particular the first 9 pages). An interesting extension is the use of *black sheep*, i.e. bad descendents from good parents, in the genetic algorithm scheme. This is discussed by Bobinger (2000)

3.4.2 Further complications of light curve fitting

Apart from the Roche geometry, various other effects are visible in the lightcurve, and depending on one's interest can be considered as unnecessary complications or interesting sources of extra information. . . We mention four of these.

The first is rapid rotation of a star, which leads to a flattened form, and thus to an altered eclipse lightcurve. It also affects the radial velocity curve: for example, when the part of the star that rotates away from us (towards us) is eclipsed, the observed radial velocity is dominated by the rotation towards us (away from us) by the part of the star that is not eclipsed, and thus shifts the radial velocity to smaller (bigger) values. This may be a noticable effect.

The second effect is the heating of a star by its companion: the radiation of one star impinges on the surface of its companion, and if sufficiently strong, heats it. When a small but hot, luminous star is accompanied by a cool star, the lightcurve may be completely dominated by the heated side facing the hot star. In this case there is only one maximum in the lightcurve per orbit, when the heated face is oriented towards Earth.

A third effect is the presence of spots. This is detectable through a variable lightcurve: as spots change their intensity and/or position, the lightcurve also changes. The spots are cooler, and therefore emit a different spectrum; the effect is largest when the spot faces the Earth, and absent when it is occulted. If a few large spots are present, their properties can be derived from careful analysis of the lightcurve and the radial velocities. However, if many weaker spots are present, they merely add noise to the lightcurve, a unique solution no longer being possible. A common procedure in such a case is to average the lightcurve over many orbits, hoping that the effects of the spots average out. . . If the Sun is any guidance, spots may also be accompanied by flares, sudden increases in the luminosity. Again, if one strong flare occurs, we can study it; if a large number of small flares occur at each time, they add irreducible noise.

A final important effect is the presence of gas streams from one star to the other,

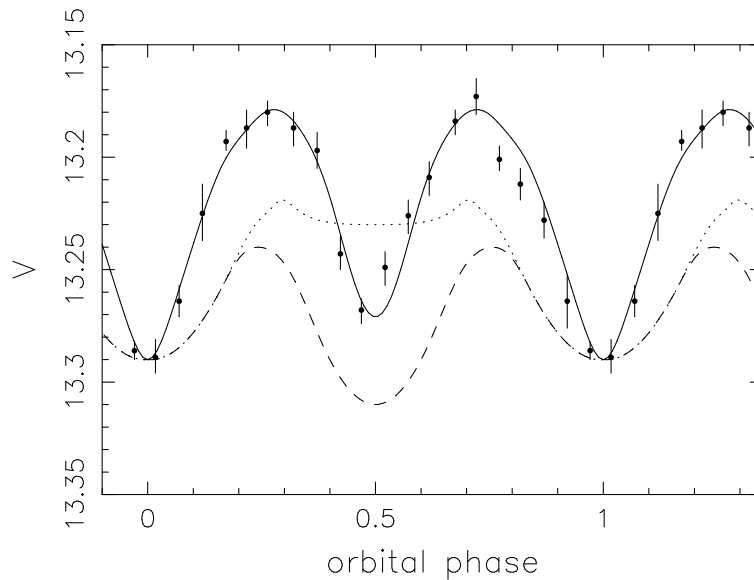


Figure 3.6: *SMC X-1* is a bright X-ray source in the Small Magellanic Cloud, in which an O star fills its Roche lobe and transfers mass via an accretion disk to a neutron star. The observed orbital light curve of *SMC X-1* (\bullet) is shown together with the predicted variations due to ellipsoidal variation only ($--$), due to ellipsoidal variation plus X-ray heating (\cdots), and due to these two effects plus an accretion disc ($—$). Note that the disk eclipses part of the heated side of the companion near phase 0.5. After Tjemkes et al. (1986).

in particular when one star fills its Roche lobe. Such a gas stream from a star that fills its Roche lobe may directly hit the other star, in particular in a close binary, or it may form a disk around the other star. Theoretically the light produced by such a stream and/or disk is not well understood. Lightcurve fitting programmes have very simplified prescriptions for gas streams and disks. In general it must be stated that the presence of a strong disk complicates the lightcurve analysis, and makes the solution less secure.

3.5 Exercises

Exercise 10. Pick a year from $1600+n20$, with n between 0 and 25, and compute the position of Castor B relative to Castor A, following the steps outlined above. Step 2 must be done iteratively. A stable method is to find two values of ε where the function $F(\varepsilon) \equiv M - \varepsilon - e \sin \varepsilon$ changes sign, and then half the interval in which this happens successively until the remaining interval is small enough for the required accuracy.

Exercise 11. Find the parallax of Castor, from the Hipparcos catalogue. Use this to compute the total mass of Castor A+B, and the radial velocity difference between the two stars at the time of Herschel's first observation.

Exercise 12. Consider the mass function Eq. 3.13. a. Show that the measurement of the velocity amplitude of star 1, K_1 , provides a lower limit to the mass of the companion M_2 .

b. What is the most likely value for the inclination?

c. In binaries with a pulsar, the analysis of the pulse arrival times gives the projected

orbital velocity of the pulsar, K_1 . To estimate the mass of the pulsar companion, one often assumes a pulsar mass $M_1 = 1.4M_\odot$, and a value for the inclination of 60° . Explain this chosen value for i .

d. PSR 1953+29 has a mass function $f(M) = 0.00272M_\odot$. Compute the mass of the companion under the assumptions listed in c).

Exercise 13. a. Rewrite Eq. 3.31 in dimensionless units, by writing all distances in units of semi-major axis a and all masses in units of M_2 , and show that the form of the Roche surfaces depends only on the mass ratio M_1/M_2 .

b. At the inner Lagrangian point, the net force is zero. Write the equation for this. Write r_2 and r_3 for the inner Lagrangian point in terms of a and r_1 . Finally, make the equation dimensionless, in the form $\mathcal{F}(r_1/a) = 0$. $\mathcal{F}(x)$ indicates 'function of x '.

c. Note: we can use the Newton-Raphson method on the dimensionless equation of b) to solve for the inner Lagrangian point. Knowing its place we can calculate its potential Φ , the potential of the Roche surface. We can derive similar equations as in b) for the second and third Lagrangian points.

Exercise 14. The radius of a $5 M_\odot$ star increases on the main sequence from $2.67 R_\odot$ to $6.52 R_\odot$. During hydrogen shell burning the radius increases to $115 R_\odot$. The companion is a $4 M_\odot$ star. Compute the maximum orbital period at which case A mass transfer occurs in this system, and the maximum orbital period for case B.

Computer Exercise 1. Write a computer code to compute the projected orbit of a visual binary, and check its correctness with your intermediate and final results in Exercise 10.

Computer Exercise 2. A binary of two brown dwarfs has the following parameters: orbital period 9.77962 d, semi-major axis $8.8 R_\odot$, eccentricity 0.333 and inclination 89.2° . The brown dwarfs have radii and effective temperatures $0.68 R_\odot$ and 2725 K for dwarf 1, $0.49 R_\odot$ and 2899 K for dwarf 2. (Thus the smaller dwarf is hotter!) In the following you may assume that the stars are spherical. The binary has a distance of 460 pc.

a. compute the flux f_I near Earth of the binary out-of-eclipse.

b. use your computer code to compute ρ as a function of orbital phase, and determine the phases during which the binary is eclipsed.

c. compute the eclipse lightcurve

Chapter 4

Fundamental parameters of stars derived from binaries

Fundamental parameters as mass, radius, luminosity and effective temperature are most accurately derived from binaries. In this chapter we discuss some examples to illustrate the derivation of such parameters, and some uncertainties inherent in these derivations, on the basis of an article on visual binaries (by Hummel et al. 1995) and an article on double-lined eclipsing binaries (by Andersen 1991). We also discuss three additional binaries to illustrate various additional methods, and the application of binary studies in distance determinations of clusters.

4.1 Visual binaries

With this section, read Hummel et al. (1995). In working the examples, we use the best parameter values; in actual scientific practice one should also propagate the errors on these parameters to errors in the derived fundamental parameters.

4.1.1 Deriving the masses: π And

Dividing the mass function for the primary (Eq. 3.13) by its equivalent for the secondary, and entering the values of K_i for π And from Table 4.1 we obtain the mass

Table 4.1: *Parameters of three binaries discussed in the article by Hummel et al. (1995) and used in the worked examples in this section. The velocity amplitudes K_i and period P are from spectroscopic observations, the eccentricity e and inclination i are from the visual orbit.*

binary:	π And	β Aur	θ Aql
K_1 (km/s)	47.5	107.75	
K_2 (km/s)	117.4	111.25	
P (d)	143.6065	3.96	17.1243
e	0.552	0.	0.607
i ($^\circ$)	103.	76.	143.5
a ($''$)	0.00669	0.0033	0.0032
f_V (10^{-12} watt m $^{-2}$ nm $^{-1}$)	0.663	6.81	2.00
f_{V1}/f_{V2}	1.45	1.20	4.09

ratio $M_1/M_2 = K_2/K_1 = 2.47$. We rewrite the mass function of the primary as

$$f(M_1) = \frac{P}{2\pi G} K_1^3 (1 - e^2)^{3/2} = M_2 \sin^3 i \frac{1}{\left(\frac{M_1}{M_2} + 1\right)^2} \quad (4.1)$$

and enter the mass ratio and the values from the visual orbit in it, to find $M_2 \simeq 12M_\odot$ and thus $M_1 \simeq 29M_\odot$. As discussed by Hummel et al. these masses are much too high to be compatible with the observed spectral type. The reason for this wrong result is probably that the value for the velocity of the secondary is spurious.

This serves as a warning that published velocities and velocity amplitudes are not always as accurate as advertised. It is always advisable to read the observational article carefully and form an informed opinion on the reliability of the results.

4.1.2 Deriving the distance: β Aur

Eq. 3.12 gives the semi-major axis of the primary; adding to this the equivalent equation for the secondary we obtain

$$a \sin i = (a_1 + a_2) \sin i = \frac{P}{2\pi} (1 - e^2)^{1/2} (K_1 + K_2) \quad (4.2)$$

Entering the values for K_i from the spectroscopic orbit and the period, eccentricity and inclination from the visual orbit of β Aur (Table 4.1) we immediately obtain the physical semimajor axis $a = 0.082$ AU, which we may compare with the semimajor axis in arcseconds from the fit of the visual orbit (Table 4.1). The combination of these two values for the semimajor axis gives the distance of the binary. Noting that $1''$ at 1 pc corresponds to 1 AU, hence that $0.0033''$ at x pc corresponds to $0.0033x$ AU, we find $x = 0.082/0.0033 = 24.8$ pc.

4.1.3 Radius and temperature: θ Aql

The visual flux f_V of θ Aql relates to the added fluxes f_{V_i} of both stars¹. The visual flux ratio has been derived from the eclipse depths (see Table 4.1). The total flux of the binary may be written

$$f_V = f_{V1} + f_{V2} = f_{V1} \left(1 + \frac{f_{V2}}{f_{V1}}\right) \quad (4.3)$$

Entering f_V and f_{V1}/f_{V2} from Table 4.1 we obtain $f_{V1} = 1.61 \times 10^{-12}$ watt m⁻² nm⁻¹.

Analogous to the example for β Aur, we can derive the distance to θ Aur as 76.9 pc, and we use this to compute the visual luminosity of the primary, $L_{V1} = 4\pi d^2 f_{V1} = 1.14 \times 10^{26}$ watt nm⁻¹ = $203L_{V\odot}$. We assume here, mainly because of the small distance, that interstellar absorption may be ignored. Deriving in the same way the blue flux f_{B1} we obtain the primary colour $f_{V1}/f_{B1} = 0.511$.

To progress from here, we must obtain the bolometric correction, i.e. the ratio of bolometric to visual luminosity (L/L_V), and the effective temperature from tabulated stellar atmosphere model spectra. Stellar atmosphere model spectra depend

¹We could also have written f_{550} , i.e. the flux at 550 nm; but we prefer f_V to indicate that the flux is a weighted average over the V-filter; we will also write U (for 365 nm), B (440 nm) and I (806 nm).

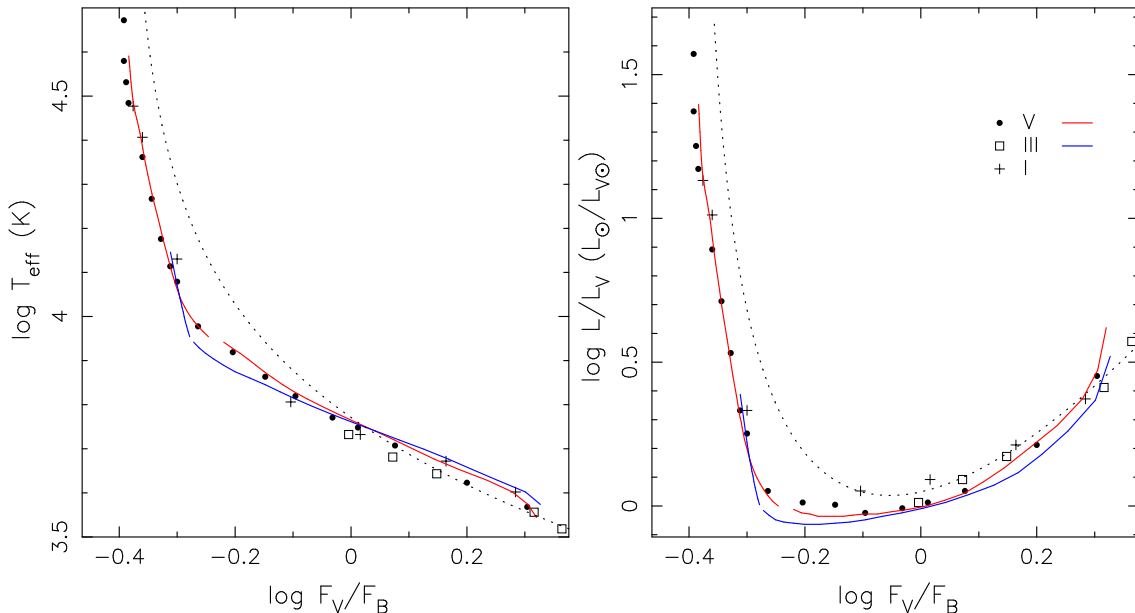


Figure 4.1: *Modern relation between colour and temperature (left) and bolometric correction (right), from Bessell et al. (1998, solid lines). For comparison some old values are also shown with symbols as indicated, from Mihalas & Binney (1981), who took their numbers from Allen (1973) and Strand (1963), who in turn compiled from others. . . . The dotted line indicate the Planck function.*

on the effective temperature T_{eff} , on the gravitational acceleration g (usually given as $\log g$), and on the metallicity (or more accurately, the abundances of all relevant elements). Hummel et al. note that both stars of θ Aql have the same colours, and use $\log L/L_V(L_\odot/L_{V\odot}) = 0.156$ and $T_{\text{eff}} = 10800$ K for both.

Thus one obtains for the primary $L_1/L_\odot = 10^{0.156} L_{V1}/L_{V\odot}$, hence $L_1 = 291L_\odot$. With

$$\log \frac{L}{L_\odot} = 2 \log \frac{R}{R_\odot} + 4 \log \frac{T_{\text{eff}}}{T_\odot} \quad \text{where} \quad T_\odot \simeq 5780 \text{ K} \quad (4.4)$$

we obtain $R_1 = 4.9R_\odot$.

In general one will find that the masses are more accurate than the luminosities or temperatures. The reason for this is one needs models to convert from colours to bolometric luminosities or effective temperatures, and that this conversion can have large uncertainty: it changes with author and with time. This is illustrated in Figure 4.1 where a modern, much used set of values are compared with those from an excellent textbook from 1981, which in turn based its tables on much older books, which in turn. . . . It is seen that at some colours, the differences are appreciable. In applying conversions with use of tables, one must also make sure to use the same calibrations for the fluxes that were used by the astronomers who compiled the tables.

4.2 Double-lined spectroscopic, eclipsing binaries

With this section, read Andersen, 1991. The extra information provided to a double-lined spectroscopic orbit by eclipses is the inclination, and through this the absolute dimensions of the stars and the binary orbit. As Andersen remarks, the

main problem in assessing uncertainties of the derived parameters are systematic errors: in practice this implies that the actual errors are rather bigger than the formal errors given by the fitting procedure.

Velocities can be measured from individual lines of known laboratory wavelength, by fitting the line profile. Problems that arise with this procedure are the possibility of blends; and the possibility that different lines arise at different depths in the atmosphere, and thus give different velocities! Balmer lines are especially troublesome; experience shows that errors as large as 30% may arise from the use of Balmer lines as the main velocity indicators. It is clearly better to use relatively narrow lines. A consequence is that velocities can be measured much less accurately for O stars than for G stars.

It is more common nowadays to determine the velocity from a cross-correlation of the observed spectrum with a template spectrum, as discussed in Chapter 1. For the template in the cross-correlation, one can use a model spectrum. Troublesome parts from the spectrum (e.g. with Balmer lines) are excluded from the cross-correlation. The advantage of this method is that the depth of the cross correlation improves not only with the correct velocity, but also with the correctness of the spectrum. This means that the cross-correlation also provides information on the parameters that set the spectrum: effective temperature, gravitational acceleration, metallicity, and rotation of the star. If no model spectrum is available, one can determine the average of all the spectra that one has taken from the object and use this as a template. In this case iteration is necessary: having determined a preliminary set of velocities, one constructs a new template by shifting all spectra to the same rest-wavelength, and then does a new cross-correlation. This procedure already converges after a few iterations.

To provide information on the temperature of the stars, the photometry must be obtained for at least two bands. A source of uncertainty is the reddening of the system. Most systems listed by Andersen are very nearby, and the reddening is small, so that the uncertainty is also small. With CCDs, photometry is often very accurate – depending on the flux of the star; the dominant uncertainty in the monochromatic luminosities is usually the distance. This means that the ratio of the monochromatic luminosities is generally much more accurate than the luminosities themselves. In Figure 4.2 the radius and luminosity are shown as a function of mass for main-sequence stars. The values come from double-lined spectroscopic eclipsing binaries. The Sun is also shown.

The radii show appreciable spread at each mass; probably mainly due to evolution. The zero-age main-sequence radius may be approximated as

$$\frac{R}{R_{\odot}} = \left(\frac{M}{M_{\odot}} \right)^n \quad (4.5)$$

where $n = 0.6$ for $M > M_{\odot}$ and $n = 1$ for $M < M_{\odot}$. The theoretical mass-radius relation for stars of sub-solar mass is still problematic. Baraffe & collaborators have shown that for low-mass stars one must incorporate full atmosphere models into the stellar structure equations to obtain a correct model.

The luminosities of main-sequence stars are well-defined as a function of mass; and may be approximated with

$$\frac{L}{L_{\odot}} = \left(\frac{M}{M_{\odot}} \right)^{3.8} \quad (4.6)$$

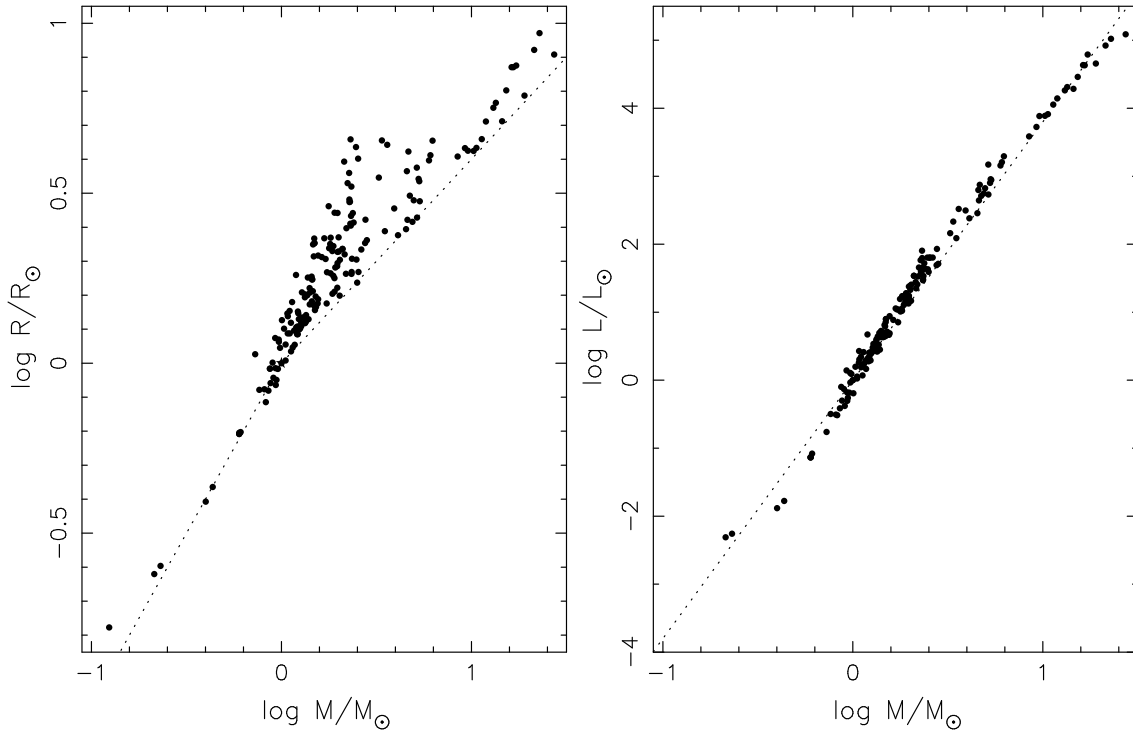


Figure 4.2: *Radius and luminosity for main sequence stars as a function of mass. Only values known with an accuracy of $\leq 2\%$ are used in this Figure. Data from Torres, Andersen & Giménez (2010); Masses and radii for HAT-TR-205-013 are added (Beatty et al. 2007), the luminosities for these very cool stars are not well-known. Dashed lines give the ZAMS mass-radius relation according to Eq. 4.5 and mass-luminosity relation according to Eq. 4.6.*

Table 4.2: *Parameters of main-sequence stars as function of spectral type. Masses, radii, luminosities and spectral type from Andersen (1991); from these, $\log g$ and T_{eff} are computed, and the colors for these parameters are found in Bessell et al. (1998). Some quantities are normalized on solar units; $L_{V\odot} = 5.6 \times 10^{23} \text{ watt nm}^{-1}$.*

SpT	M (M_{\odot})	R (R_{\odot})	$\log L$ (L_{\odot})	T_{eff} (K)	$\log L_V$ ($L_{V\odot}$)	$\log L/L_V$ ($L_{\odot}/L_{V\odot}$)	$\log f_B/f_U$	$\log f_V/f_B$	$\log f_I/f_V$
Main sequence									
O8V	22.0	7.90	5.10	38900	3.71	1.39	-0.68	-0.38	-0.66
B2V	9.0	4.30	3.63	22400	2.77	0.86	-0.57	-0.35	-0.63
B5V	5.0	2.90	2.66	15600	2.16	0.49	-0.46	-0.33	-0.60
A0V	2.5	1.80	1.51	10200	1.42	0.09	-0.25	-0.27	-0.56
A5V	1.9	1.50	1.06	8590	1.08	-0.02	-0.19	-0.22	-0.50
F0V	1.5	1.30	0.67	7420	0.71	-0.04	-0.22	-0.15	-0.41
F5V	1.3	1.20	0.43	6800	0.46	-0.03	-0.23	-0.10	-0.35
G0V	1.2	1.10	0.30	6470	0.33	-0.03	-0.22	-0.07	-0.32
G5V	1.0	1.00	0.00	5780	0.00	0.00	-0.15	0.01	-0.25
K0V	0.9	0.85	-0.33	5180	-0.39	0.06	-0.01	0.08	-0.18
M1V	0.6	0.55	-1.22	3860	-1.64	0.42	0.28	0.29	0.12
M4V	0.4	0.40	-1.87	3110	-2.80	0.92	0.29	0.35	0.56

From the mass, radius and luminosity one may compute the gravitational acceleration g and effective temperature T_{eff} of the atmosphere; and from atmosphere models (which are calibrated with accurately measured stars) one may then obtain the absolute monochromatic luminosities and colours. The results are given in Table 4.2.

For very cool objects, the bolometric corrections are unknown; for very-low-mass stars and brown dwarfs, observers derive absolute monochromatic luminosities, rather than effective temperatures or bolometric luminosities. For such stars, instead of the mass-luminosity relation, one has the mass-monochromatic-luminosity $M-L_\lambda$ relation.

4.3 Some interesting binaries

In this section we discuss binary studies that illustrate variants on the analysis methods discussed above, and that are interesting for a variety of reasons. The binary HAT-TR-205-013 illustrates the use of rotational velocity in the determination of the parameters of the lowest-mass main-sequence star. The binary 2MASSJ05352184-0546085 gives the parameters of two brown dwarfs. The binary HD 23642 gives the distance to the Pleiades. We give brief descriptions here, and refer to the original papers for more detail. The variant techniques are flagged in the margin.

4.3.1 The lowest main-sequence mass: HAT-TR-205-013 B

One of the methods to detect planets around other stars is to look for transits of the planet. If a planet has a radius R_p and passes in front of the star with radius R , a fraction $(R_p/R)^2$ of the stellar surface is covered, and flux that we detect is reduced accordingly. Analysis of the transit lightcurve provides information on the limb darkening of the star.

Interestingly, a Jupiter-like planet has a size comparable to that of low-mass main-sequence stars, and some candidate planets found from transits turn out to be stars of spectral type late M. They are easily distinguished from planets because they cause much larger variations in the radial velocity of the primary.

In the case of HAT-TR-205-013, Beatty et al. (2007) determine the parameters of the late dwarf, as follows. (HAT stands for Hungary-made Automated Telescope; to discover transits a network of six 11 cm telescopes is used, see Bakos et al. 2004; 205 is the number of the survey field.) The parameters determined first are a , a_1 , R_2 , R_1 , and i . The transit lightcurve provides three relations between these parameters. Roughly speaking, the length of the eclipse in units of the orbital period depends mostly on R_1/a , the eclipse depth on R_2/R_1 , and the lengths of ingress and egress on $s = a \cos i$, the closest projected distance of the star centers ². (See Exercise 16 and Figure 4.3.) A fourth relation is given by the radial velocity curve of star 1, which shows that $e = 0$, and gives $a_1 \sin i$ (see discussion leading to Eq. 3.13). If star 2 contributes significantly to the spectrum, its radial velocity provides the fifth relation between the parameters. Here, however, star 2 is not seen in the spectrum, and the required fifth relation is found from the observed (i.e. projected) rotation velocity $v_{\text{rot,o}}$ of star 1. *It is assumed that the rotation of star 1 is locked to the orbit,*

*rotation
velocity*

²Beatty et al. write this in dimensionless form, with $b \equiv s/R_1$

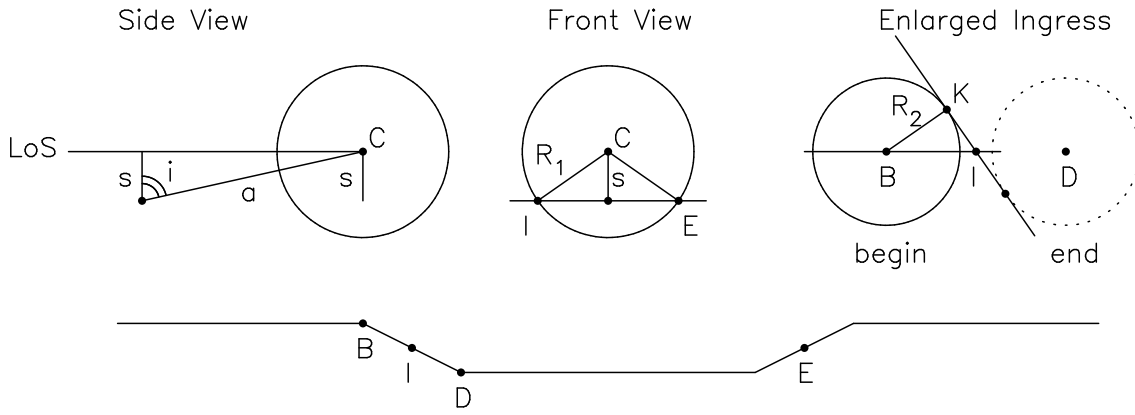


Figure 4.3: *Slightly simplified geometry to show the effect of the impact parameter s on form of the transit lightcurve. The left graph shows the definition of s : it is the shortest projected distance of the center of star 2 to the center of star 1. LoS is the line of sight towards the Earth, and a the distance between the stars. The middle graph shows the path of star 2 in front of star 1; it is simplified (assuming $R_1 \ll a$) because in reality the path between ingress I and egress E should be slightly curved (part of an ellipse if the orbit is circular), with the pericenter in the middle. The ingress is shown in more detail in the right graph, where the line through IK is the edge of the star; the short stretch of the circular edge is approximated with a straight line (assuming $R_2 \ll R_1$). The resulting lightcurve is shown schematically in the lower graph. As the center of star 1 moves along BD, ingress starts (ends) at B (D), where its projected circle first (last) touches the edge of star 1. Mid-ingress is at I. Since BID is along IE (see middle graph), and BK is parallel to IC, we have $s/R_1 = KI/BI = \sqrt{1 - (R_2/BI)^2}$. This shows that the length of ingress, proportional to BI, depends on s . For $s = 0$ $BI = R_2$. (For s close to 1 the approximation that the edge of the star is a straight line breaks down.)*

Table 4.3: *Measured quantities and parameters of the binary HAT-TR-205-013, from Beatty et al. (2007).*

a/R_1	5.9(1)	$M_1 (M_\odot)$	1.04(13)
R_2/R_1	0.1309(6)	$M_2 (M_\odot)$	0.124(10)
$s/R_1 = a \cos i/R_1$	0.37(5)	$R_1 (R_\odot)$	1.28(4)
$v_{\text{rot}} \sin i$ (km/s)	29(1)	$R_2 (R_\odot)$	0.167(6)
K_1 (km/s)	18.3(5)	$a (R_\odot)$	7.5(3)
P (d)	2.23074(1)		
e	0		

hence $v_{\text{rot}} = \Omega R_1 = (2\pi/P)R_1$, hence

$$v_{\text{rot,o}} = v_{\text{rot}} \sin i = \frac{2\pi}{P} R_1 \sin i \quad \Rightarrow \quad \frac{P}{2\pi} v_{\text{rot,o}} = R_1 \sin i \quad (4.7)$$

Once the parameters a , a_1 , R_2 , R_1 , and i are determined, the total mass and the individual masses can be found with Kepler's third law, Eq. 2.45, and from the ratio a_1/a .

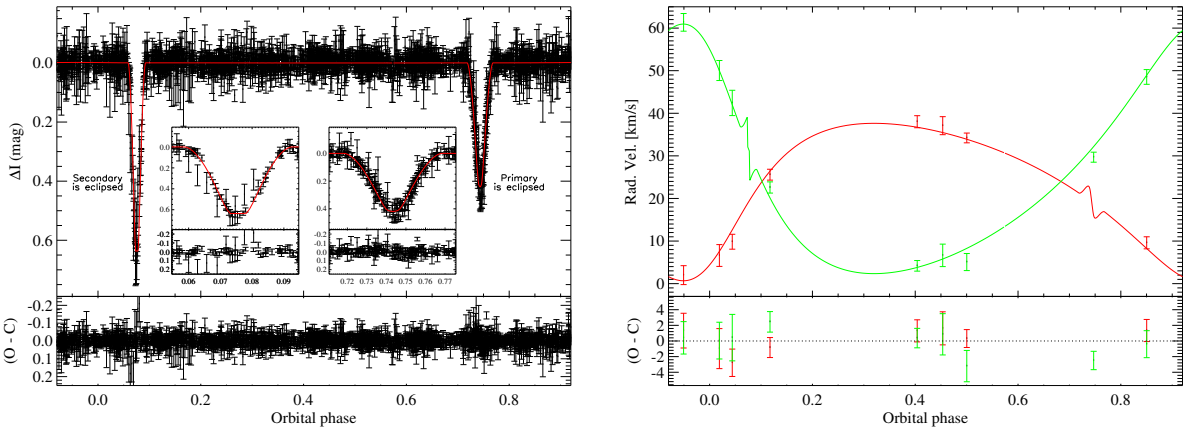


Figure 4.4: *Eclipse lightcurve and radial velocity curve of the brown dwarf binary 2MASSJ05352184–0546085. Note the effect of ingress and egress on the theoretical radial velocity curve of the eclipsed star. From Stassun et al. (2007)*

Table 4.4: *Parameters of the brown-dwarf binary 2MASSJ05352184–0546085 and of the Pleiades binary HD 23642 (Stassun et al. 2007, Groenewegen et al. 2007)*

	2MASS	HD		2MASS	HD
K_1 (km/s)	18.5(7)	99.2(3)	M_1 (M_\odot)	0.057(5)	2.22(3)
K_2 (km/s)	29.3(8)	140.8(3)	M_2 (M_\odot)	0.036(3)	1.57(2)
P (d)	9.77962(4)	2.4611335(7)	R_1 (R_\odot)	0.68(2)	1.84(4)
e	0.333(6)	<0.002	R_2 (R_\odot)	0.49(2)	1.59(4)
i ($^\circ$)	89.2(2)	77.6(2)	L_1 (L_\odot)	0.022(2)	
a (R_\odot)	8.8(2)	11.95(2)	L_2 (L_\odot)	0.015(2)	
T_2/T_1	1.064(4)	0.768(4)	T_1 (K)	2725	9950

4.3.2 The brown-dwarf binary 2MASSJ05352184–0546085

Cool stars and brown dwarfs are best discovered in the infrared. The 2μ All Sky Survey is an efficient source for new discoveries of such objects. Stassun et al. (2007) analyse an eclipsing binary in the Orion Nebula Cluster. Radial velocities are measured through a technique of Broadening Functions, which is a variant of the cross-correlation technique; it works better when the velocity difference between the stars is comparable to the resolution of the observed spectra (Rucinski 1999). The broad-band I light curve is analysed assuming that the surfaces of the stars radiate as black bodies. Radial velocities and lightcurve are analysed with the Wilson-Devinney code, and give the parameters listed in Table 4.4.

broadening functions

A first remarkable result is that the brown dwarfs are rather large for their mass: this can be understood by their young age. The Orion Nebula Cluster is thought to be ~ 1 Myr old, and in this time brown dwarfs have not relaxed to their equilibrium radius.

A second remarkable result is that the less massive star is hotter: this follows immediately from the observation that the eclipse of the less massive star is deeper. Since the temperatures of both stars are almost equal, it is unlikely that this result is the consequence of the difference between real brown-dwarf atmosphere spectra and Planck spectra. Stassun et al. suggest that the lower temperature of the primary can be explained if it is ~ 0.5 Myr older than the secondary.

Membership of the Orion Nebula is in agreement with the systemic radial velocity (γ) of the binary: 24.1(4) km/s, compared to the velocity 25.0 ± 1.5 km/s of the cluster. It is also in agreement with the distance derived from the luminosity and spectrum. The spectral type M6.5 for the primary implies (through measurements of the M6.5 star LHS 292) a temperature of 2725 K, and a bolometric correction $L/L_K = 3800$ (the K-band is around $2\mu\text{m}$). The temperature of the secondary is found from T_2/T_1 . The luminosities of the stars derived from their radii and effective temperatures are given in the Table. The bolometric flux can be derived from the K-band out-of-eclipse flux $f_K = 1.59 \times 10^{-18} \text{ watt m}^{-2} \text{ nm}^{-1}$ and the bolometric correction. Comparison of these numbers gives the distance of the binary as 456 ± 34 pc, compatible with the distance to the Orion nebula of 480 ± 80 pc.

4.3.3 The distance to the Pleiades from binary HD 23642

The distance to the Pleiades determined by the HIPPARCOS mission was a big surprise: it was significantly closer (116(3) pc) than results found from main-sequence fitting (about 130 pc). If correct, the HIPPARCOS distance implies that the main sequence of the Pleiades is 37% fainter than the main sequence of stars near the Sun!

The binary HD 23642 has been studied to resolve this discrepancy: it is a member of the Pleiades, and by determining its distance one also determines the cluster distance.

Groenewegen et al. (2007) first use cross-correlation techniques of model spectra with the observed spectra to derive the temperatures and effective gravities of both stars, and to derive their radial velocities as a function of phase. The fit to radial velocities and lightcurves then provides the other binary parameters listed in Table 4.4.

The distance is determined by comparing model fluxes in different filters with observed fluxes. In general, for a star with radius R at distance d , the flux observed on Earth f_λ is related to the flux leaving 1 m^2 of the stellar surface through:

$$4\pi R^2 F_\lambda = 4\pi d^2 f_\lambda \quad (4.8)$$

We know the observed flux f_λ and from the fitting also the radius R , thus if we can determine F_λ we have the distance. This determination can be done for either star separately, or for the out-of-eclipse flux of the binary as a whole.

Groenewegen et al. use two methods to determine F_λ . In Method A one uses a stellar atmosphere *model*, determined by the stellar temperature, $\log g$ and metallicity, to compute the flux F_λ at wavelength λ for 1 m^2 at the stellar surface. In Method B one uses an *empirical relation* between the effective temperature and F_λ , or alternatively between the colour and F_λ . Groenewegen et al. use the colours f_V/f_B and f_K/f_V . In both cases, a correction for interstellar absorption towards the Pleiades must be made. The distance obtained for HD 23642 is 138.0 ± 1.3 pc.

*colour-flux
relation*

The consensus nowadays is that the HIPPARCOS distance is not correct.

4.4 Exercises

Exercise 15. Use the Hipparcos catalogue to find the parallaxes of β Aur and θ Aql, and compare with the distances derived from the visual orbit and observed fluxes.

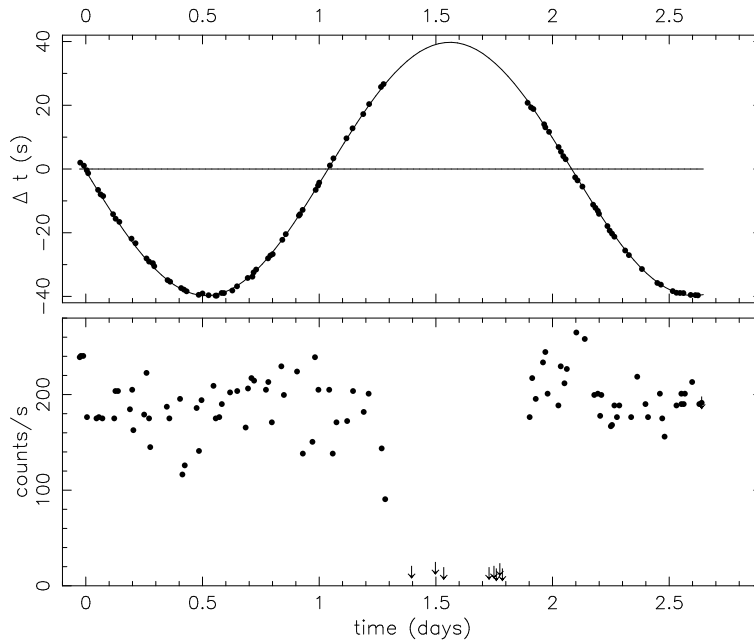


Figure 4.5: *Below: the X-ray intensity observed from Cen X-3 (dots, upper limits indicated with arrows); above: the time difference Δt between the observed pulse arrival time and the arrival time predicted for a constant pulse period.*

Which distances are most accurate?

Exercise 16. Use the measured quantities listed in the left-hand column of Table 4.3, to derive the binary parameters given in the right-hand side.

Exercise 17. We use the mass function $f(M)$ for a circular orbit to study the parameters of the high-mass X-ray binary Cen X-3: a binary in which an X-ray pulsar is in orbit around a high-mass star. Consider a binary of stars with masses M_1 and M_2 , and orbital period P_b . The orbit is circular, the orbital inclination (i.e. the angle between the line of sight from the Earth and a line perpendicular to the orbital plane) is i . The radial velocity of star 1 has been determined, and it varies as a sine wave, with amplitude K_1 . The mass function for a circular orbit is

$$f(M) \equiv \frac{M_2^3 \sin^3 i}{(M_1 + M_2)^2} = \frac{4\pi^2}{G} \frac{(a_1 \sin i)^3}{P_b^2} = \frac{K_1^3}{2\pi G} P_b \quad (4.9)$$

where a_1 is the semi-major axis of the orbit of star 1 with respect to the center of mass.

a. In Figure 4.5 we see some data of Cen X-3. A sine wave describes the time arrival times well, i.e. the orbit is circular. The orbital period is 2.087 days, the amplitude of the time-delay curve is 39.7466 s. Compute the mass function of Cen X-3. Show that the mass function provides a lower limit to the mass of the companion of the X-ray pulsar.

b. We see that the neutron star is eclipsed by its O star companion. t is the eclipse length. Assume that the O star is a sphere (i.e. ignore its deformation by tidal forces) and show that the ratio of the radius of the O star R to the radius of the orbit a is given by

$$\frac{R}{a} = \sqrt{1 - \cos^2 \left(\frac{\pi t}{P_b} \right) \sin^2 i} \quad (4.10)$$

c. We can use Eq. 4.10 to determine R/a from t/P_b , as a function of i . Assuming that the donor fills its Roche-lobe, we can use Eq. 3.33 to determine the mass ratio M_1/M_2 , and then from Eq. 4.9 both masses separately. Determine t/P_b from Fig. 4.5, and calculate M_1 and M_2 for inclinations of 70° and 90° . Note that the masses of the neutron star are rather small. This is due in part by our neglect of the deformation of the O star by tidal forces.

Chapter 5

Tidal forces

Tidal forces lead to a coupling in the binary of the spin of the stars with the orbital revolution. If energy is dissipated, angular momentum can be exchanged between the orbit and the spin of the stars.

We discuss some aspects of this with use of three articles

- Hut (1980) shows on the basis of a general analysis that the minimum energy situation of a binary is reached if the angular momenta of the orbit and of the two stars are aligned, and if both stars corotate with the orbit, i.e. their rotation period equals the binary period
- Hut (1981) gives simple analysis of the effect of the deformation of a star on the evolution of the binary orbit, and provides a good physical insight into the tidal forces. We examine only the first 5 pages of this article, which give the outline.
- Verbunt (2007) discusses the evolution of the rotation of the Earth and of the revolution of the Moon as driven by the spin-orbit coupling.

5.1 Exercises

Exercise 18a. Compute the total angular momentum of a binary consisting of two stars with masses $M_{1,2}$ and radii $R_{1,2}$, and how that it can be separated into the angular momentum of the orbit and the angular momenta of the two stars around their own axes of rotation. Start from Eq. 2.42, assume that the stars are perfectly spherical, and save on computing by clever use of anti-symmetry. The orbital angular velocity is Ω , the angular velocities of the stars around their own axes are $\omega_{1,2}$.

b. Consider synchronous rotation, $\Omega = \omega_1 = \omega_2$ and derive the condition for which the rotation of the two stars around their own axes can be neglected.

Exercise 19. (After Counselman, C. 1973, ApJ 180, 307.) Two stars with masses M and m , with $M \gg m$, orbit one another in a circular orbit with angular velocity n . The star with mass M also rotates around its own axis with angular velocity ω and its moment of inertia is kMR^2 . We consider the orbital energy and angular momentum, i.e. ignore the kinetic energy and angular momentum of the center of mass.

a. Compute the total angular momentum L' and the total energy E' of this binary

system, expressed in m, M, n and ω . Define:

$$\sigma^2 \equiv \frac{GM}{R^3}; \quad \kappa \equiv \left(\frac{m}{kM}\right)^{1/4} \left(1 + \frac{m}{M}\right)^{1/6}$$

$$\Omega \equiv \frac{\omega}{\sigma} \kappa^{-3}; \quad N \equiv \left(\frac{n}{\sigma}\right)^{1/3} \kappa^{-1}$$

and show

$$L \equiv \frac{L'}{kMR^2\kappa^3\sigma} = \Omega + N^{-1}; \quad E \equiv \frac{E'}{kMR^2\kappa^6\sigma^2} = \frac{1}{2} (\Omega^2 - N^2)$$

b. sketch lines of constant E in the N - Ω plane for $E = 0, 0.5, -0.5$; and for constant L for $L = 0, 1, 2, -1, -2$. Argue from this sketch that the location where a line of constant angular momentum is tangent to a line of constant energy corresponds to an extremum of energy for fixed angular momentum. This implies that the tangent point is an equilibrium situation. Show that in such a point $\Omega = N^3$, i.e. $\omega = n$ (synchronous rotation). Sketch this line in the figure as well.

c. compute in the equilibrium point from b):

$$\left(\frac{\partial E}{\partial N}\right)_{L=\text{const}} \quad \text{and} \quad \left(\frac{\partial^2 E}{\partial N^2}\right)_{L=\text{const}}$$

When is the equilibrium of synchronous rotation stable?

Bibliography

- [1] C.W. Allen. *Astrophysical quantities*. Athlone Press, London, 1973.
- [2] J. Andersen. Accurate masses and radii of normal stars. *A&A Review*, 3:91–126, 1991.
- [3] T. Beatty, J. Fernandez, D. Latham, and et al. The mass and radius of the unseen M-dwarf companion in the single-lined eclipsing binary HAT-TR-205-013. *ApJ*, 663:573–582, 2007.
- [4] M.S. Bessell, F. Castelli, and B. Plez. Model atmospheres broad-band colors, bolometric corrections and temperature calibrations for O-M stars. *A&A*, 333:231–250 (Erratum: 337, 321), 1998.
- [5] A. Bobinger. Genetic eclipse mapping and the advantage of Black Sheep. *A&A*, 357:1170–1180, 2000.
- [6] P. Charbonneau. Genetic algorithms in astronomy and astrophysics. *ApJS*, 101:309–334, 1995.
- [7] C. Counselman. Outcomes of tidal evolution. *ApJ*, 180:307–316, 1973.
- [8] M. Groenewegen, L. Decin, M. Salarsi, and P. De Cat. The Pleiades eclipsing binary HD 23642 revisited. *A&A*, 463:579–587, 2007.
- [9] W.D. Heintz. The Castor system. *PASP*, 100:834–838, 1988.
- [10] C.A. Hummel, J.T. Armstrong, D.F. Buser, D. Mozurkewich, A. Quirrenbach, and M. Vivekanand. Orbits of small angular scale binaries resolved with the MARK III interferometer. *AJ*, 110:376–390, 1995.
- [11] P. Hut. Stability of tidal equilibrium. *A&A*, 92:167, 1980.
- [12] P. Hut. Tidal evolution of close binary systems. *A&A*, 99:126–140, 1981.
- [13] D. Mihalas and J. Binney. *Galactic astronomy. Structure and kinematics*. Freeman, San Francisco, 1981.
- [14] J. Orosz and P. Hauschildt. The use of the `nextgen` model atmospheres for cool giants in a light curve synthesis code. *A&A*, 364:265–281, 2000.
- [15] W.H. Press, S.A. Teukolsky, W.T. Vetterling, and B.P. Flannery. *Numerical Recipes: The Art of Scientific Computing²*. Cambridge U. P., Cambridge, 1992.
- [16] É. Roche. Recherches sur les atmosphères des comètes. *Annales de l’Observatoire imperial de Paris*, 5:353–393, 1859.

- [17] S. Rucinski. Determination of broadening functions using the singular value decomposition (SVD) technique. In J.B. Hearnshaw and C.D. Scarfe, editors, *Precise stellar radial velocities*, ASP Conference Series 185, pages 82–90. ASP, San Francisco, 1999.
- [18] K.G. Stassun, R.D. Mathieu, and J.A. Valenti. A surprising reversal of temperatures in brown-dwarf eclipsing binary 2MASS J05352184–0546085. *ApJ*, 664:1154–1166 (erratum: 674, 615), 2007.
- [19] K.A. (ed.) Strand. *Basic Astronomical Data*. University of Chicago Press, Chicago, 1963.
- [20] G. Torres, J. Andersen, and A. Giménez. Accurate masses and radii of normal stars: modern results and applications. *Ann.Rev.A.A.*, 18:67–126, 2010.
- [21] F. Verbunt. *The Earth and the Moon: from Halley to lunar ranging and shells*. www.astro.uu.nl/~verbunt/onderwijs/binary/earth.pdf, Utrecht, 2007.
- [22] H. Von Zeipel. The radiative equilibrium of a rotating system of gaseous masses. *MNRAS*, 84:665–684, 1924.
- [23] R.E. Wilson and E.J. Devinney. Realization of accurate close-binary light curves: application to MR Cygni. *ApJ*, 166:605–619, 1971.